# InletTracker: An open-source Python toolkit for historic and near real-time monitoring of coastal inlets from Landsat and Sentinel-2

Valentin Heimhuber[1], Kilian Vos[1], Wanru Fu[1], and William Glamore[1]

[1]UNSW Sydney

November 22, 2022

**Abstract**

Despite their global abundance and high ecological and socio-economic significance, the dynamics of coastal inlets often remain poorly quantified at multi-decadal time scales. Here, we introduce InletTracker, a new tool that reconstructs the time-evolving state of dynamic coastal inlets over the last 30+ years from publicly available Landsat 5, 7 and 8 and Sentinel 2 satellite imagery. InletTracker is a Google Earth Engine enabled python toolkit that uses a novel least cost pathfinding approach to trace inlets along and across the berm (i.e., barrier, bar), and then analyses the resulting transects to infer whether an inlet is open or closed. To evaluate the performance of InletTracker, we applied the tool at 12 intermittent coastal inlets with different maximum inlet widths ([?]30-200m), geomorphological setting and opening frequency located across Southeastern and Southwestern Australia. This exercise involved 6363 unique binary inlet state predictions (i.e., open vs. closed) that were validated against visually inferred inlet states (from the satellite imagery itself), on-ground observational records, and in situ water levels from inside the inlets. InletTracker reproduced the visually inferred inlet states with an average accuracy across all sites of 89% for the combined Landsat and Sentinel 2 record (15-30m resolution) and 94% for the Sentinel 2 record only (10m resolution). Overall, we found good agreement between the predictions of the tool and the three independent validation datasets for all but the smallest sites. Our results demonstrate that InletTracker will enable coastal engineers, managers, and researchers to gain new insights into the dynamics and drivers of coastal inlets or similar shallow water landforms such as river mouths, tidal flats, floodplains, wetlands or delta channel networks. Further, the high spatial (i.e., 10m) and temporal (i.e., 5 daily) resolution provided by Sentinel 2 makes InletTracker a viable option for near real-time monitoring of even relatively small inlets with a minimum channel width of around 10m and frequent, short duration, openings.

# InletTracker: An open-source Python toolkit for historic and near real-time monitoring of coastal inlets from Landsat and Sentinel-2

**Valentin Heimhuber[1]*, Kilian Vos[1], Wanru Fu[1], William Glamore[1]**

[1] Water Research Laboratory, School of Civil & Environmental Engineering, UNSW Sydney, NSW 2052, Australia

*Correspondence: v.heimhuber@unsw.edu.au

**Abstract:**

Despite their global abundance and high ecological and socio-economic significance, the dynamics of coastal inlets often remain poorly quantified at multi-decadal time scales. Here, we introduce InletTracker, a new tool that reconstructs the time-evolving state of dynamic coastal inlets over the last 30+ years from publicly available Landsat 5, 7 and 8 and Sentinel-2 satellite imagery. InletTracker is a Google Earth Engine enabled python toolkit that uses a novel least-cost pathfinding approach to trace inlets along and across the berm (i.e., barrier, bar), and then analyses the resulting transects to infer whether an inlet is open or closed. To evaluate the performance of InletTracker, we applied the tool at 12 intermittent coastal inlets with different maximum inlet widths (≤30-200m), geomorphological setting and opening frequency located across Southeastern and Southwestern Australia. This exercise involved 6363 unique binary inlet state predictions (i.e., open vs. closed) that were validated against visually inferred inlet states (from the satellite imagery itself), on-ground observational records, and in situ- water levels from inside the inlets. InletTracker reproduced the visually inferred inlet states with an average accuracy across all sites of 89% for the combined Landsat and Sentinel-2 record (15-30m resolution) and 94% for the Sentinel-2 record only (10m resolution). Overall, we found good agreement between the predictions of the tool and the three independent validation datasets for all but the smallest sites. Our results demonstrate that InletTracker will enable coastal engineers, managers, and researchers to gain new insights into the dynamics and drivers of coastal inlets or similar shallow water landforms such as river mouths, tidal flats, floodplains, wetlands or delta

channel networks. Further, the high spatial (i.e., 10m) and temporal (i.e., 5 -daily) resolution provided by Sentinel-2 makes InletTracker a viable option for near real-time monitoring of even relatively small inlets with a minimum channel width of around 10m and frequent, short-duration, openings.

**Keywords:** Tidal inlets, ICOLL, barrier breach, Google Earth Engine, remote sensing, least-cost pathfinding, coastal monitoring, intermittent estuaries

## 1. Introduction

### 1.1 Background

Many of the world's coastlines feature highly dynamic intermittent/ephemeral coastal inlets (also referred to as tidal inlets, entrances, mouths) that close when fluvial or tidal flows are insufficient to prevent coastal sediments from infilling the inlet channel via longshore drift, aeolian transport, and wave processes (Haines et al., 2006; Hayes and FitzGerald, 2013; McSweeney et al., 2017; Moore and Murray, 2019; Otvos, 2020; Roy et al., 2001; van Ormondt et al., 2020). These intermittent coastal inlets can substantially influence the hydrodynamics, morphology and ecology of often extensive sheltered estuarine/lagoon environments on the landward side of the inlet (Velasquez Montoya et al., 2018), which provide numerous ecosystem services including storm protection, carbon sequestration, recreation and fisheries productivity (Moore and Murray, 2019; Newton et al., 2018; Scanes et al., 2020). Examples of intermittent coastal inlets include those that form after major coastal storms at barrier island systems, such as the Outer Banks of North Carolina, U.S. (Moore and Murray, 2019; van Ormondt et al., 2020; Velasquez Montoya et al., 2018), or those found at the downstream end of over 1477+ documented intermittent estuaries worldwide (McSweeney et al., 2017).

Due to the often sporadic and erratic nature of intermittent coastal inlets, they remain less understood than more mature and permanent coastal inlets (Behrens et al., 2013; Mcsweeney et al., 2018; Velasquez Montoya et al., 2018), pose a challenge for coastal management (Alluvium, 2012; Gordon and Nielsen, 2020; Stephens and Murtagh, 2012) and sometimes feature a heated socio-political debate around management interventions such as mechanical openings/closures (Gladstone et al., 2006; Gordon and Nielsen, 2020; Stephens and Murtagh, 2012; Young et al., 2014). These concerns can be compounded by a lack of datasets on historic inlet states (open vs. closed), which, apart from a few targeted coastal monitoring programs (e.g., DPIE (2020a)), do not exist for many inlets around the globe. To this end, publicly available satellite records such as the Landsat and Sentinel-2 (S2) archives hold great potential for reconstructing coastal inlet dynamics (i.e., location, frequency, duration, size and evolution of openings/closures) over the last 30+ years.

Information on the long-term spatial and temporal dynamics of coastal inlets would enable researchers to further advance the existing knowledge on the mechanics and drivers of inlet opening/closure (e.g., Behrens et al., 2013; Bertin and Mendes, 2019; González-Villanueva et al., 2017; Mcsweeney et al., 2018; Mcsweeney and Stout, 2020; Morris and Turner, 2010; Ranasinghe and Pattiaratchi, 2003; Slinger, 2017; van Ormondt et al., 2020; Velasquez Montoya et al., 2018), the hydrology (e.g., Gale et al., 2007) and ecology (e.g., Gladstone et al., 2006; Scanes et al., 2020) of intermittent estuaries, or the impacts of climate change on coastal inlet dynamics (e.g., Duong et al., 2016; Duong et al., 2017, 2018). To date, however, the potential of satellite remote sensing remains poorly explored and there is need for an automated and transferable method to monitor intermittent coastal inlets worldwide. To address this need, this paper introduces InletTracker, a Google Earth Engine (GEE) enabled (Gorelick et al., 2017), open-source python software package for historical and near real-time monitoring of highly dynamic and/or intermittent coastal inlets.

### 1.2 Existing methods for monitoring coastal inlets

Existing monitoring and survey techniques for coastal inlets include RTK-GPS and echo-sounding surveying (e.g., Mcsweeney and Stout (2020); Morris and Turner (2010)), stationary coastal imaging systems such as Argus (e.g., Harley et al. (2011)) as well as more recent techniques such as UAVs (Turner et al., 2016) and airborne water penetrating LiDAR (Kinsela et al., 2020). While these techniques are suitable for surveying coastal inlets at a high resolution, they remain costly and their suitability for reconstructing historical inlet dynamics depends on when corresponding surveys were initiated.

In the absence of long-term observational data, process understanding of intermittent coastal inlets is often obtained via numerical, empirical or conceptual models (e.g., Baldock et al. (2008); Duong et al. (2018); McSweeney et al. (2018); Morris and Turner (2010); Slinger (2017); van Ormondt et al. (2020); Velasquez Montoya et al. (2018); Wainwright et al. (2013)). Although such models typically require extensive field data for calibration and validation, they can potentially be used to reconstruct

historical inlet dynamics (Duong et al., 2016). Alternatively, a few studies have applied remote sensing for reconstructing inlet dynamics (Bertin and Mendes, 2019; Scanes et al., 2020). Notably, Scanes et al. (2020) used the *Water Observations from Space* 25-year time series of Landsat-based binary surface water masks (Mueller et al., 2016) to infer a number of past openings of Nadgee Lake on the east coast of Australia from variations in the surface water extent of the estuary.

In addition, several related image processing algorithms target features with geomorphological and spectral characteristics similar to those of coastal inlets. For instance, a number of studies have applied a waterline mapping approach to reconstruct the extent, dynamics or elevation surface of intertidal flats (Bishop-taylor et al., 2019; Bishop-Taylor et al., 2019; Murray et al., 2019; Ryu et al., 2008; Sagar et al., 2017; Son et al., 2020). Another closely-related body of research is concerned with mapping the location and/or dynamics of shorelines (Bishop-taylor et al., 2019; Liu and Yang, 2009; Pardo-pascual et al., 2012; Sanchez-García et al., 2020; Vos et al., 2019a; Zhao et al., 2008). Both algorithm groups typically map the waterline on individual images as accurately as possible, while also accounting for the tide level at image capture. Robust shoreline detection algorithms, such as those employed by CoastSat (Vos et al., 2019b), SHOREX (Sanchez-García et al., 2020), or NIDEM (Bishop-Taylor et al., 2019) have been shown to provide waterlines at sub-pixel accuracy, but they are ultimately not designed for identifying intermittent coastal inlet states, where the modulation of ocean tides, variations in water composition and complex branching of channel networks limit their application.

Another group of relevant algorithms is concerned with the satellite-based mapping of planform river channel geometry and morphodynamics (Chen et al., 2020; Gong et al., 2020; Isikdogan et al., 2015; Monegaglia et al., 2018; Rowland et al., 2016; Schwenk et al., 2017) and an overview is provided in Rowland et al. (2016). Methods with proven skill for mapping shallow delta and tide channel networks include the algorithms of Isikdogan et al. (2017, 2015) and Gong et al. (2020).

While these algorithms represent major advancements for automated mapping of changes in beach width and stream channel characteristics from publicly available satellite imagery, they are ultimately not suitable to detect whether an inlet is open or close. Here, we introduce InletTracker, a novel

remote sensing technique capable of automatically mapping the evolution of highly-dynamic intermittent coastal inlets from Landsat and S2 imagery. InletTracker employs a least-cost pathfinding technique to trace inlet channels and locates their bottleneck consistently through multi-decadal imagery records. The purpose of this paper is to illustrate the skill and limitations of InletTracker, based on a comprehensive validation exercise involving 12 intermittent coastal inlets in Australia with varying inlet channel width and geomorphological setting. Section 2 describes the methodology behind InletTracker and details the experiments used for evaluating its performance. The results are provided in Section 3 and discussed in Section 4, which is followed by the conclusions in Section 5.

## 2. Materials and methods

### 2.1 Proposed method: InletTracker

The three 'core challenges' to infer the state of an intermittent coastal inlet from medium resolution multispectral satellite imagery are:

i) The dynamic nature of inlet channels, which can dramatically change over time and space.
ii) The high variability in reflectance over coastal inlets in the spatial (i.e., dynamic features such as shallow channels, sand bars, mudflats, seagrass and adjacent vegetation) and temporal (i.e., changes in water colour through seasons, periods of opening and closure, ebb and flood tide cycles) domains.
iii) The shallow water areas in and around coastal inlets that may alternate between wet and dry phases depending on the, which is often further compounded by the potentially small size of inlet channels relative to the resolution of the satellite imagery.

The motivation behind InletTracker was to develop an automated tool for tracking the time-evolving location and state (i.e., open vs. closed) of coastal inlets that could address these challenges as efficiently as possible, while also being applicable across a wide range of geomorphological settings. InletTracker consists of a series of integrated Python codes that are freely available on Github (https://github.com/VHeimhuber/InletTracker) and Mendeley Data (Heimhuber et al., 2021), where detailed guidance is provided on the installation and use of the tool. A high-level overview of the InletTracker method, its architecture and major processing steps is provided in Figure 1.

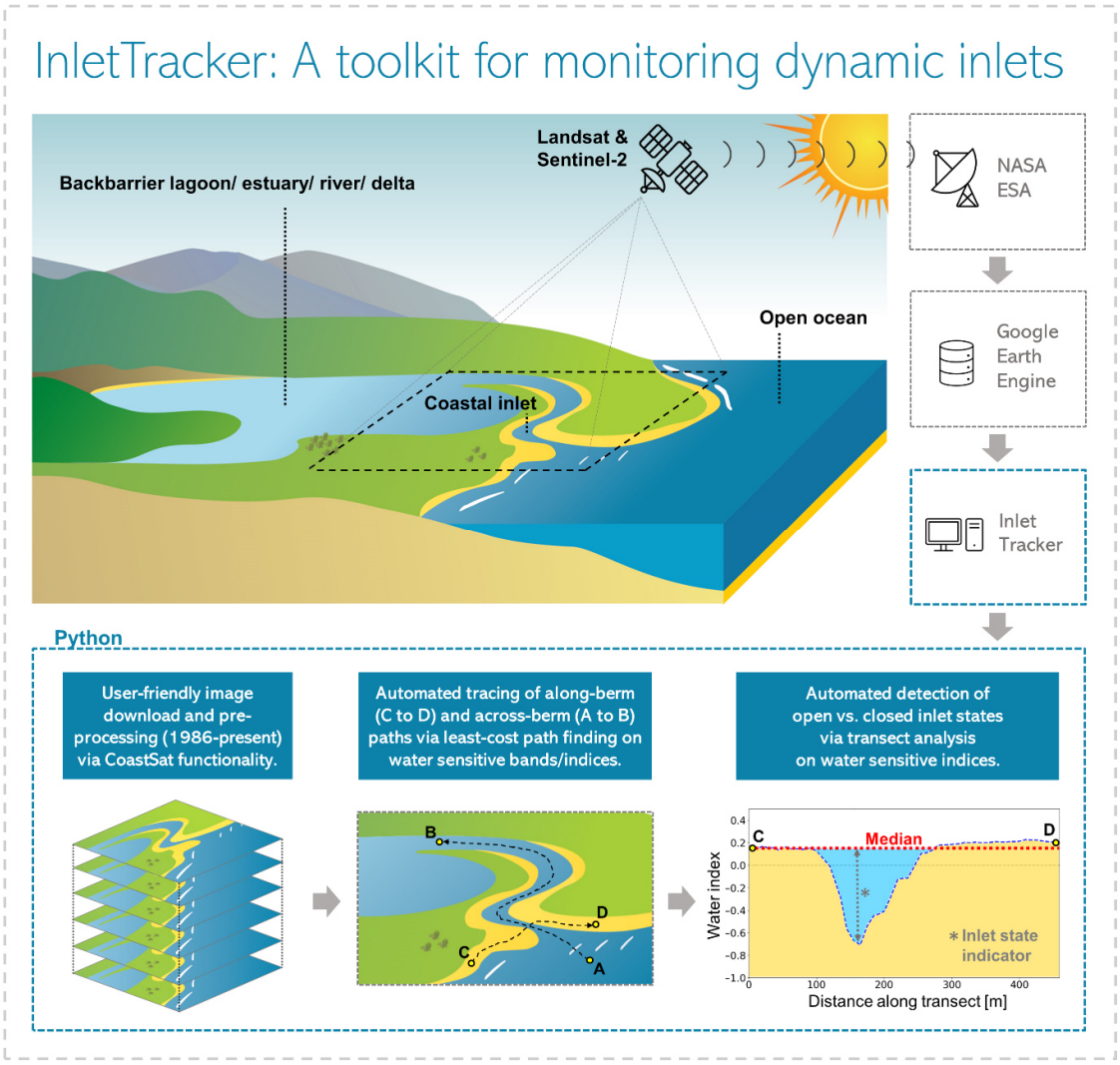


**Figure 1:** Conceptual diagram illustrating the architecture and key processing steps of InletTracker.

The sequence of computations provided by InletTracker can be summarized as follows:

i) Image download and pre-processing;

ii) Least-cost pathfinding along and across the berm (i.e., barrier, bar);

iii) Inferring open vs. closed inlet states.

In the following sections, each of these steps is described in detail and an emphasis is placed on how each of the three aforementioned challenges is addressed.

### 2.1.1 Image download and pre-processing

InletTracker uses functionality of the CoastSat python toolbox (Vos et al., 2019b) to access publicly available optical satellite data through the GEE. Briefly, the toolbox retrieves Landsat 5, 7 & 8 (L5, L7, L8) and S2 Top-of-Atmosphere images cropped to a user-defined region of interest before pre-processing to mask cloudy pixels and enhance spatial resolution (pansharpening/downsampling) to achieve a common resolution of 15m/pixel across all bands for Landsat and 10m/pixel for S2.

### 2.1.2 Least-cost pathfinding

To address the rapid changes in inlet channel location and shape (core challenge 1), a least-cost pathfinding technique is used to automatically trace two distinct paths on each image (see also Figure 1):

i) The deepest path connecting a point in the open ocean (referred to as A) with a point inside the estuary (B) as shown in Figures 1 and 2a. The A-B pass is hereafter referred to as the across-berm path.

ii) The path connecting two points on the beach berm on opposite sides of the inlet channel through the shortest and shallowest (i.e., bottleneck) section of the channel. This path connects points C and D in Figures 1 and 2a and is hereafter referred to as along-berm path.

The automated tracing of these paths for each image is implemented via the least-cost algorithm of the scikit-image graph module (Van Der Walt et al., 2014). The algorithm iteratively routes through a 'cost surface' in the form of two-dimensional grid from the seeds (A and C) to the receiver points (B and D), accumulating the cost of every pixel along the path. The resulting least-cost path is the one that has the lowest cumulative cost. This pathfinding problem is similar to finding the shortest route connecting two points in a road network, where the cost of each road segment is the time required to drive it. Instead of the travel time, however, InletTracker uses a single image band or index that is proportional to the depth of water as the cost surface. This allows it to find the deepest connection (i.e., least-cost) between points A and B and the shallowest connection (i.e., maximum cost) between

points C and D. The user can choose between the NIR, SWIR1, the Normalized Difference Water Index (NDWI) ((Green-NIR)/(Green+NIR)) (Mcfeeters, 1996) or the modified NDWI (mNDWI) ((Green-SWIR1)/(Green+SWIR1)) (Xu, 2007) as the cost surface for least-cost pathfinding. In addition, two user-defined polygons are used to specify the search region for finding the across and along-berm paths (see Figure 2a). This range of options for the cost surface partially addresses the spatial and temporal variability in reflectance over coastal inlets (core challenge 2). Further, to overcome issues with the least-cost path taking shortcuts over parts of the beach, as illustrated in Figure 2b, the cost surface was exponentiated by a factor of 25. This exponentiation exaggerates the cost for crossing dry pixels and thereby, encourages the algorithm to trace along wet pixels, even if this results in a substantially longer path (see Figure 2c).

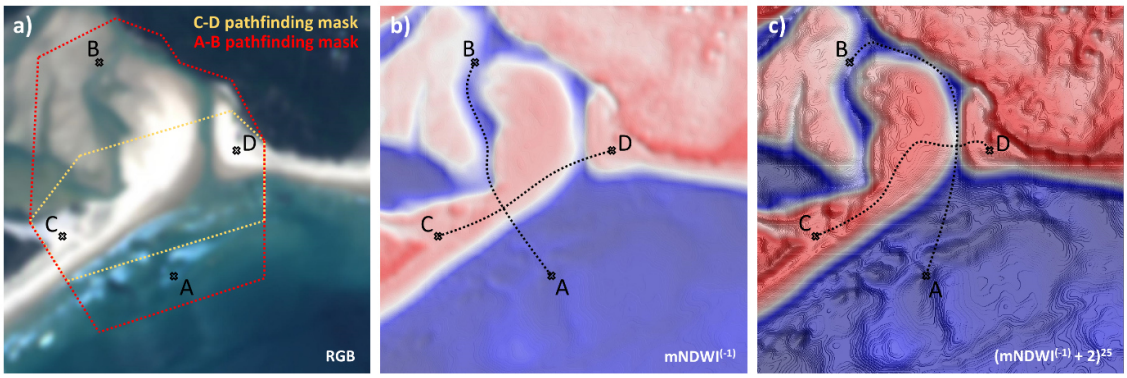


**Figure 2:** Illustration of the least-cost pathfinding method showing (a) S2 true color image (14.02.2018) with seed (A and C) and receiver (B and D) points and masks for pathfinding; (b) $mNDWI^{(-1)}$ plotted as an elevation surface; (c) the 'amplified' $mNDWI^{(-1)}$ cost surface obtained via $(mNDWI^{(-1)}+2)^{25}$. For the unmodified $mNDWI^{(-1)}$ cost surface (b), taking a short cut over the beach berm results in a lower cumulative cost than tracing through the inlet for the across-berm (A-B) path. After amplification (c), across-berm pathfinding consistently locates the inlet channel centreline along the deepest flow path, while along-berm pathfinding tends to approach the bottleneck of the inlet channel.

The along-berm and across-berm paths obtained via pathfinding reduce the spectral information over the area of interest to only what is relevant for distinguishing between an open vs. a closed inlet state. Although the limited resolution of the satellite imagery relative to the potentially small size of inlet

channels (core challenge 3) is a physical limitation inherent to the input data, this 'focusing' ensures that any available information is used efficiently to infer the state of the inlet.

#### 2.1.3 Inferring open vs. closed inlet states

The pathfinding method presented in the previous section consistently traces the along-berm and across-berm paths for images in a multi-temporal time series. The second major step of the method is to use the information obtained via pathfinding to automatically infer whether an inlet is open or closed. To this end, either NDWI or mNDWI is extracted in its original form (i.e., without exponentiation but inversed so that water features become negative) along each transect in 1m intervals. Figure 3 illustrates this method based on Landsat 8 images of an intermittent inlet in south-eastern Australia (Lake Conjola) during an open (Fig. 3a) and closed inlet state (Fig. 3b). The $mNDWI^{(-1)}$ extracted along the across-berm and along-berm transects are shown in panels (c) and (d) respectively for the open image and in (e) and (f) for the closed image.

An open inlet, such as the one shown in Figure 3a, creates distinct features in the along-berm and across-berm transects. For open inlets, the across-berm transects typically display very low values for the open ocean part of the path starting at Point A, before showing a local maximum near the intersection with the along-berm transect (Figure 3c). After the local maximum, the transect typically continues at lower values but with more variability, due to shallow channel and sandbar features inside the inlet. The local maximum near the intersection typically corresponds to the point of lowest water depth in the inlet channel (see section S3 in the supplementary materials for details). Conversely, the along-berm transects commonly provides high values over the dry sand areas on either end of the path, with a local minimum near the intersection with the across-berm transect (Figure 3d). Since these transects are based on water-sensitive bands or indices, these local maxima or minima are of particular importance for inferring inlet states. In most inlet configurations, the local maximum of the across-berm and the local minimum of the along-berm transect are identical. In a closed state (Figure 3b, e, f), they both exhibit the mNDWI of dry sand, which, in this example, is

slightly above 0.2. During open states, the magnitude of the local maximum/minimum depends on the state of the inlet and the tide, with the most negative values being obtained for deep inlet channels captured during high tide. Conversely, for inlets that are either very small or just about to close and captured during low tide, the local maxima/minima tend to approach those of dry sand.

To distinguish between an open or a closed inlet, the method then uses a threshold. However, rather than applying a single threshold to the entire local maxima or minima series, the accuracy of which can be strongly affected by even minor variations in lighting or atmospheric conditions from image to image, InletTracker uses an alternative approach. As can be seen in Figure 3d, the majority of the along-berm transect is located over the beach berm, which typically exhibits very stable mNDWI/NDWI values of dry sand. Through a series of experiments, we found that the median of the along-berm transect consistently approaches the mNDWI or NDWI of dry sand for a wide range of inlet configurations. The key advantage of this approach is that no prior knowledge of the spectral signature of the beach berm or initial classification step is required. Instead, the spectral signature of the dry parts of the berm is established automatically for every image.

Based on these learnings, the detection of inlet states in InletTracker is implemented as follows:

i) First, the local maxima and minima are identified for each image based on the location of the intersection of the across-berm and along-berm transects and a user defined search window (defined as a search distance on either side of the intersection) (see Figure 3c and d).

ii) Next, the difference between the local maximum or minimum and the median of the along-berm transect is calculated (hereafter referred to as the $\Delta$-to-median parameter).

iii) Lastly, a single threshold is applied to distinguish between open (above threshold) and closed (below threshold) inlet states. The optimal classification threshold is site specific and can be inferred based on a user-generated set of training data consisting of visually inferred inlet states. This training data generation is readily implemented in InletTracker via an interactive user interface.

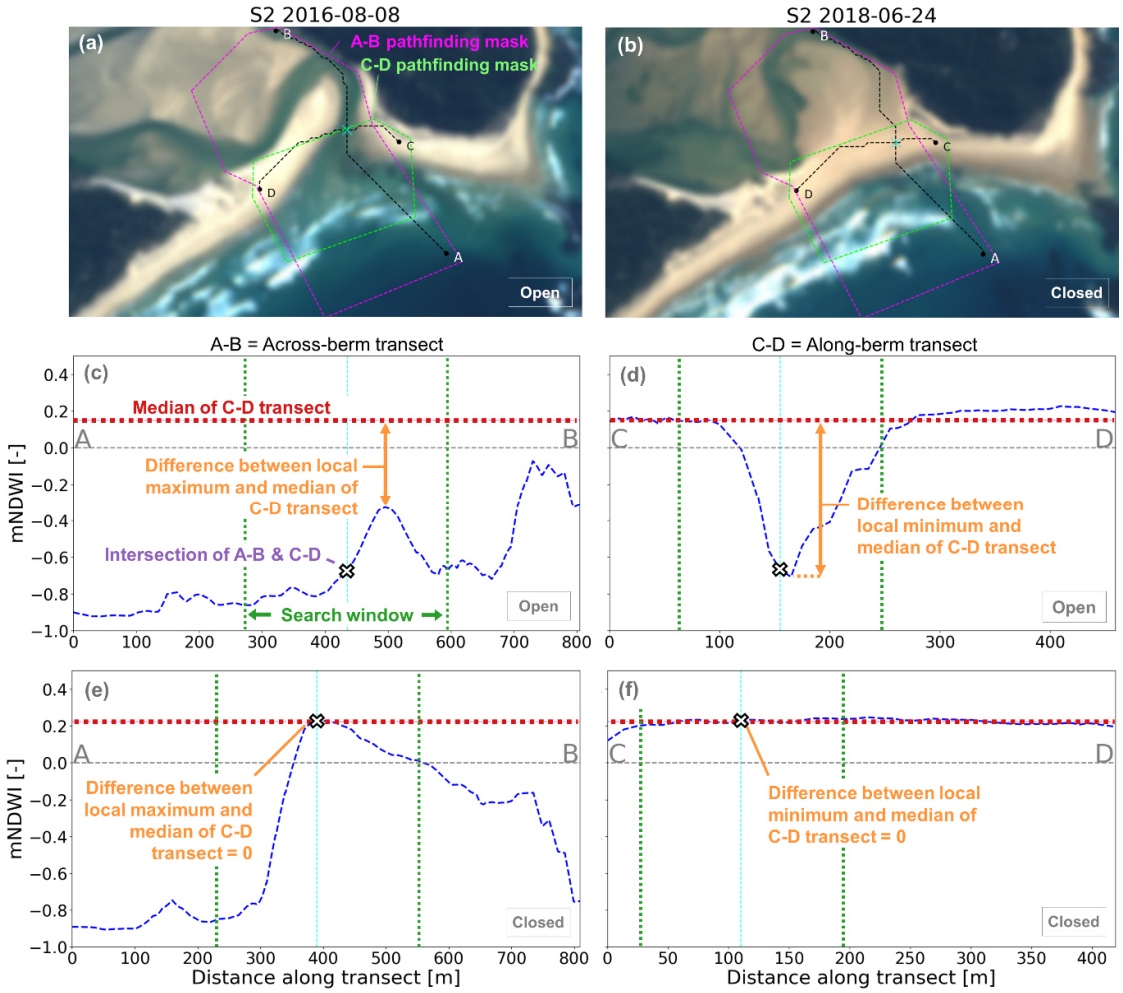


**Figure 3:** Illustration of the method used for automated detection of inlet states in InletTracker, where (a) and (b) are S2 images for Lake Conjola during an open and closed inlet state respectively. Also shown are the user defined seed (A/C) and receiver (B/D) points for pathfinding, the corresponding masks for limiting the search area, and the automatically traced across-berm and along-berm paths. Panels (c) and (d) show the across-berm and along-berm $mNDWI^{(-1)}$ transects for the open image, while (e) and (f) show the same transects for the closed image. Based on these transects, the method uses a search window to find the maximum of the across-berm and minimum of the along-berm path in the vicinity of the intersection between the two paths. It then calculates the difference between the median of the along-berm transect and the local maximum/minimum (Δ-to-median) and uses this parameter as a proxy of the inlet state.

### 2.2. Validation

To test its performance, we first applied InletTracker to reconstruct the inlet dynamics of 12 test sites in two distinct configurations, which are representative of how the tool will likely be used by different users. For the first configuration, we used the full L5, 7 and 8 and S2 imagery record and used SWIR1 for pathfinding and the mNDWI for inferring inlet states. In the second configuration, we used only the S2 imagery and used NIR for pathfinding and NDWI for inferring inlet states. This second configuration takes advantage of the 10m vs. 15m resolution of the NIR vs. the SWIR1 band of S2 that could provide better detection accuracy for small inlets. We then compared the results against three independent datasets, namely i) visually-inferred open vs. closed inlet states for all available cloud free Landsat and S2 images ii) long-term observational records of open vs. closed inlet states available for four of the sites (DPIE, 2020a) and iii) in-situ water level data for the estuaries of seven of the 12 inlets (DPIE, 2020b). Additionally, we generated additional results to illustrate the effects of the tide as well as the different band and index options provided by the tool (see S3 in supplementary materials). In the following sections, the three validation exercises are explained in detail.

#### 2.2.1 Test sites

We selected 12 intermittent coastal inlets in Australia with different estuary waterbody and inlet sizes, geomorphological settings, and inlet dynamics (Figure 4). For each site, the seed and receiver points for along-berm and across-berm pathfinding along with the corresponding boundary masks are shown. We used Wamberal, Coila, Conjola and Durras for a focused illustration of the results since these sites had consistent long-term observational records. Table 1 provides an overview of the key characteristics of each site. Like all intermittent estuaries, they have low or seasonally-low fluvial inflows, a spring tidal range of less than 2.50 m and a deep-water significant wave height averaging 1.25 m or higher (data not shown) (Mcsweeney et al., 2017).

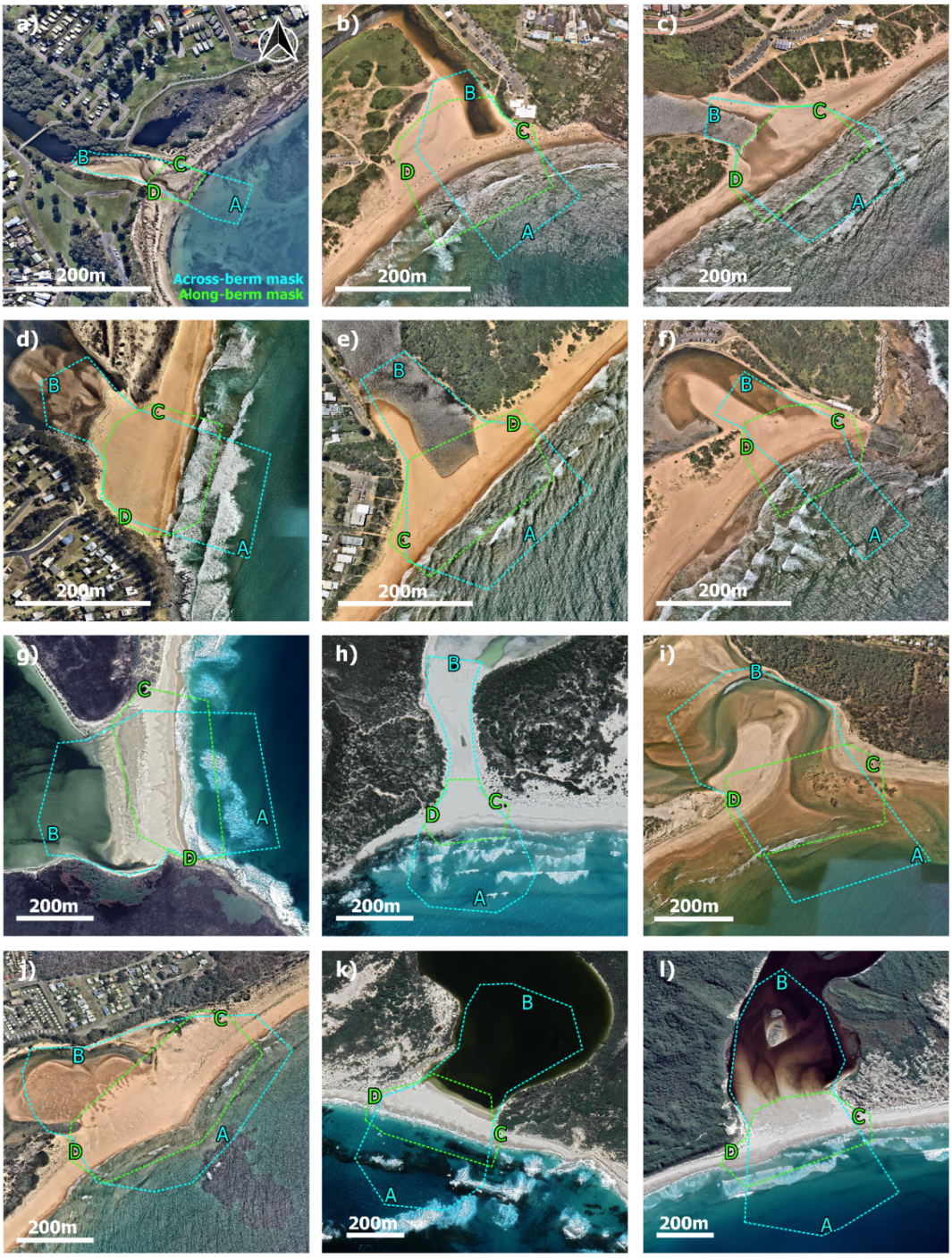


**Figure 4:** Location and inlet configuration of the 12 study sites in Australia showing the across-berm (A to B) and along-berm (C to D) seed and receiver points and corresponding masks used to limit the area for pathfinding. Sites are ordered from small to large and site names are (a) Inman River, (b) Curl Curl, (c) Dee Why, (d) Coila, (e) Wamberal, (f), Narrabeen, (g) Nadgee, (h) Hamersley Inlet, (i) Conjola, (j) Durras, (k) Stokes Inlet, (l) Irwin Inlet. The coordinates of each site are provided in Table 1. Background images are from Nearmaps.

As can be seen in Figure 4, the approximate berm width of these sites ranges from under 50m for the smallest site (Inman River) to around 400m for the largest sites (e.g., Conjola, Stokes Inlet, Irwin Inlet). Approximate inlet closure indices (i.e., the proportion of time the inlet is closed) ranged from 0.17 for Narrabeen to 0.96 for Wamberal (Haines, 2006).

**Table 1:** Location and key characteristics of the 12 inlets used for testing the performance of InletTracker. [1] = Carmichael (2000); [2] = Roper et al. (2011); [3] = Chuwen et al.( 2009); [4] = Department of Water (2007); [5] = Calculated from model data of Lyard et al. (2020); [6] = Haines (2006) ; [7] = Google Earth Pro

| Inlet name | Point A Lat; Long | Min. inlet opening width/ Distance C to D (m) | Catchment size (km²) | Estuary area (km²) | Annual rainfall (mm) | Mean tidal range (m) | Inlet closure index |
|---|---|---|---|---|---|---|---|
| Inman River | -35.562381; 138.613905 | ≤30 [7] / 65 | 195.5 [1] | 0.034 | 712 [1] | 0.69 [5] | - |
| Curl Curl | -33.768373; 151.299358 | ≤30 [7]/ 185 | 4.65 [2] | 0.063 | 1151 [2] | 1.24 [5] | 0.8 [6] |
| Dee Why | -33.747558; 151.304552 | ≤60 [7]/ 270 | 4.27 [2] | 0.311 | 1146 [2] | 1.24 [5] | 0.7 [6] |
| Coila | -36.050623; 150.142422 | ≤60 [7]/ 200 | 47.64 [2] | 7.071 | 806 [2] | 1.18 [5] | 0.95 [6] |
| Wamberal | -33.430613; 151.449385 | ≤70 [7] / 260 | 5.82 [2] | 0.503 | 1124 [2] | 1.25 [5] | 0.96 [6] |
| Narrabeen | -33.70493; 151.309039 | ≤70 [7]/ 140 | 52.41 [2] | 2.266 | 1108 [2] | 1.24 [5] | 0.17 [6] |
| Nadgee | -37.468075; 149.97493 | ≤60-90[7]/ 560 | 13.7 [2] | 1.226 | 808 [2] | 1.15 [5] | 0.8 [6] |
| Hamersley Inlet | -33.970127; 119.907729 | ≤70[7]/ 200 | 1610 [3] | 2.653 | 500 [3] | 0.54 [5] | - |
| Conjola | -35.271437; 150.510819 | ≤70[7]/ 380 | 139.09 [2] | 6.436 | 951 [2] | 1.20 [5] | 0.4 [6] |
| Durras | -35.640561; 150.308009 | ≤90[7]/ 560 | 58.38 [2] | 3.650 | 944 [2] | 1.19 [5] | 0.62 [6] |
| Stokes Inlet | -33.856799 121.133298; | ≤200[7]/ 470 | 4500 [4] | 12.110 [4] | 550 [4] | 0.56 [5] | - |
| Irwin Inlet | -35.024153; 116.95796 | ≤200[7]/ 480 | 2343 [3] | 12.574 [3] | 623 [3] | 0.47 [5] | - |

### 2.2.2 Validation against visually inferred binary inlet states

Due to a lack of alternative datasets that cover the full Landsat record, visual analysis of the input imagery was the only feasible option for assessing performance across all sites over the full imagery record. The previously mentioned InletTracker training data generator randomly shuffles through the available cloud free images of a site, providing a focused view of the inlet in true color, the NDWI, and the mNDWI. The analyst then chooses between 'open', 'closed', 'unclear' or 'poor quality' via arrows on the keyboard. 'Unclear' is selected if the inlet is neither clearly open or closed, while 'poor quality' is selected if there is significant cloud cover, cloud shadow or haze present in the direct vicinity of the inlet. A total of 4933 images (excluding unclear or poor-quality) were visually classified into open and closed inlet states for this validation and 'unclear' images were excluded from the analysis.

Since the entire set of visually inferred validation data was generated by a single analyst, we conducted an additional experiment to test the representativeness of this data. To this end, training data was generated by an additional six analysts with a background in coastal science for the full S2 record at Conjola and Dee Why. From these six validation datasets, we then calculated the majority vote. This majority vote was then compared against the single analyst data for all overlapping image dates, which revealed agreement levels of 82% for Dee Why and 87% for Conjola. This illustrates that there is a degree of bias in the visually inferred binary entrance states that needs to be carefully considered in the interpretation of the results.

To evaluate the performance of the algorithm, the binary inlet states inferred from the along-berm and across-berm $\Delta$-to-medians were compared against the visually inferred binary inlet states, based on the accuracy and F1-score metrics (see Section S1 in the supplementary materials on details how these are calculated). The time series of $\Delta$-to-median parameters was classified into open vs. closed inlet states using the threshold that resulted in the highest F1-score. Consequently, the resulting accuracies could be slightly higher than those that would be obtained based on a smaller set of training data.

#### 2.2.3 Validation against observational inlet states

In New South Wales, Australia, records of open vs. closed inlet states are collected for some inlets and centrally maintained by the Department of Primary Industries and the Environment (DPIE, 2020a). The time period and quality of this data varied considerably across the test sites. Here, only the observational records for the four focus sites, which had consistent long-term records, were used. Importantly, the observational records are not perfect as they are often based on several different sources of information and data collection methods. For several occasions, the dataset contained question marks, empty fields or vague remarks for certain inlet openings or time periods. If a date was provided for only the day of opening or the day of closing, then a duration of one month was applied to complete the dataset.

#### 2.2.4 Validation against in-situ water level data

Lastly, the InletTracker results were compared against the degree of tidal attenuation. Due to the limited hydraulic conveyance capacity of inlet channels, ocean tides are significantly attenuated in landward water bodies of inlets (González-Villanueva et al., 2017; Gordon and Nielsen, 2020; Haines, 2006; McPherson et al., 2013; Slinger, 2017). The degree of tidal attenuation of a particular inlet depends, among other less significant factors, on the size of the inlet opening as well as the size of the estuarine waterbody and its corresponding tidal prism (Khojasteh et al., 2020; Young et al., 2014). Since the surface water area of an estuary is roughly constant through time, the level of tidal attenuation is largely a function of the size of the inlet opening. Here, we estimated the degree of tidal attenuation by comparing the tidal range inside the estuaries with the tidal range in the open ocean as exemplified for Durras in Figure 5.

Water levels inside an intermittent estuary can vary substantially within a single day in response to heavy rainfall during closed inlet states as seen in Figure 5a. To account for these non-tidal water level fluctuations, we first calculated the difference between the minimum and the maximum water level for each day, and then selected the minimum daily value along a 3-day rolling window (Figure 5b).

For the open ocean, tide data from the FES2014 global ocean tide atlas (Lyard et al., 2020), a finite element solution global ocean tide model that is readily integrated with InletTracker was used. The data was extracted from the model based on the location of seed points A for each site (see Table 1) and the tidal range was then calculated as the difference between the daily maximum and minimum (Figure 5b). Tidal attenuation of each inlet was then calculated using Equation 1 (Figure 5c).

*Tidal attenuation = (1 – (Tidal range inside the inlet / Tidal range in the open ocean)) * 100* (Eq.1)

Since both the Δ-to-median parameter and tidal attenuation are somewhat proportional to the degree of opening of an inlet, there should be some correlation between these two parameters. To test this, we calculated correlation statistics (Pearson correlation coefficient, and p-value) between the Δ-to-median parameter and tidal attenuation for seven sites for which in-situ water level data was available.

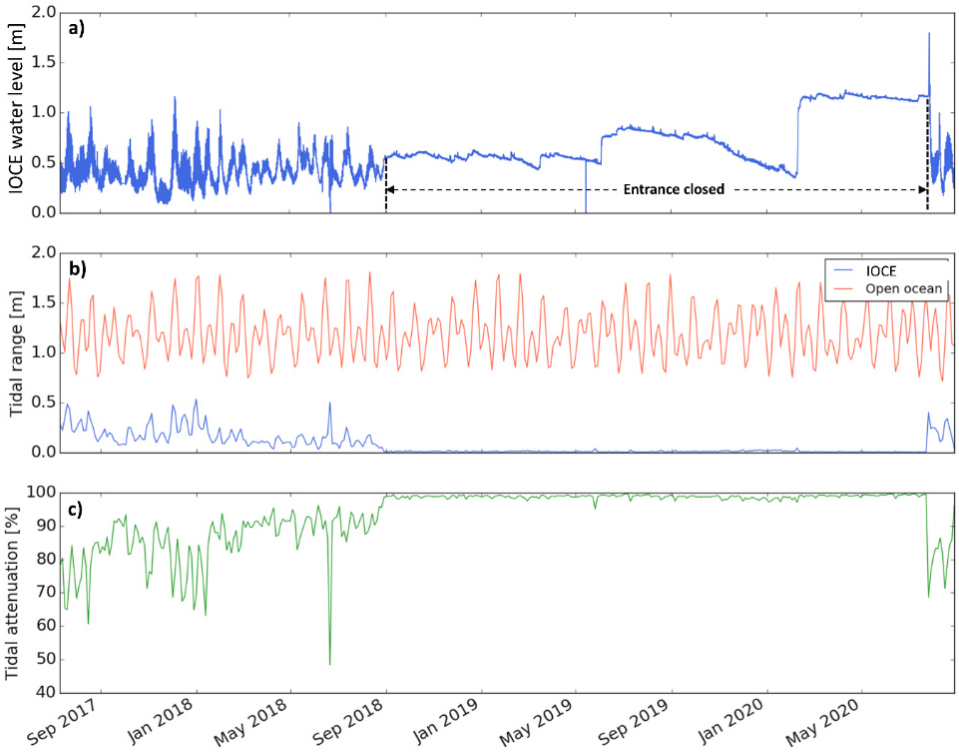


**Figure 5:** Illustration of how tidal attenuation from the open ocean into the estuary was calculated, here exemplified for Durras Lake, NSW. Shown are a) water levels as measured by a gauge inside the inlet; b) tidal range in the open ocean as predicted by the FES global tide model (red) (Lyard et al., 2020) and in the lagoon inferred from the water level data (blue) (DPIE, 2020b); c) tidal attenuation obtained via dividing the estuary tidal range by the open ocean tidal range.

## 3. Results

### 3.1 Pathfinding

Overall, InletTracker was found to have excellent ability for consistently tracing dynamic inlet channels along and across the berm. This is exemplified in the pathfinding results for selected S2 images during an ~8 month opening sequence of Inman River, South Australia (Figure 6). The image series illustrates the dramatic variations in water level, water color, sun angle (i.e., see increased brightness over the beach berm during summer months), and channel and wave condition that can accompany the opening and closure of inlet inlets. The pathfinding algorithm effectively dealt with these complexities and correctly identified the desired across-berm and along-berm paths along with their intersection around the bottleneck of the inlet opening. Further, since pathfinding was based on the NIR band for S2 in this example, the obtained paths tend to avoid white water, which has high reflectance in the NIR range.

The ability to consistently trace inlet channels is further illustrated by the results obtained for the full S2 record, which, for Durras, comprised 75 cloud free images during open (as inferred visually) and 58 images during closed inlet states (Figure 7). Panels a, b, c and d in Figure 7 show the corresponding paths (one path per image), grouped by the direction of pathfinding and state of the inlet. Here, and in the remainder of this manuscript, orange and red tones represent closed inlet states, while blue tones represent open inlet states. The across-berm transects during open inlets (panel c) illustrate considerable variability in the location and shape (e.g., sinuosity) of inlet openings. The across-berm transects during closed inlet states tend to cross the beach berm at its narrowest part but are otherwise not of further value. Both the open and closed along-berm paths provide an indication of the average position and dynamics of the beach berm throughout the satellite record.

Panels e) and f) in Figure 7 show the mNDWI values extracted from the S2 imagery along the across-berm and along-berm paths and illustrate the usefulness of the pathfinding approach. For the 133 S2 images, the transects consistently depict distinct features for open and closed inlet states. For open

inlet states, the along-berm transects exhibit the characteristic channel cross section shape (panel e), while the across-berm transects consistently show lower maxima for the berm crossing. As with the 2-d planform paths, these transects hold considerable information that can facilitate a detailed assessment of inlet morphodynamics.

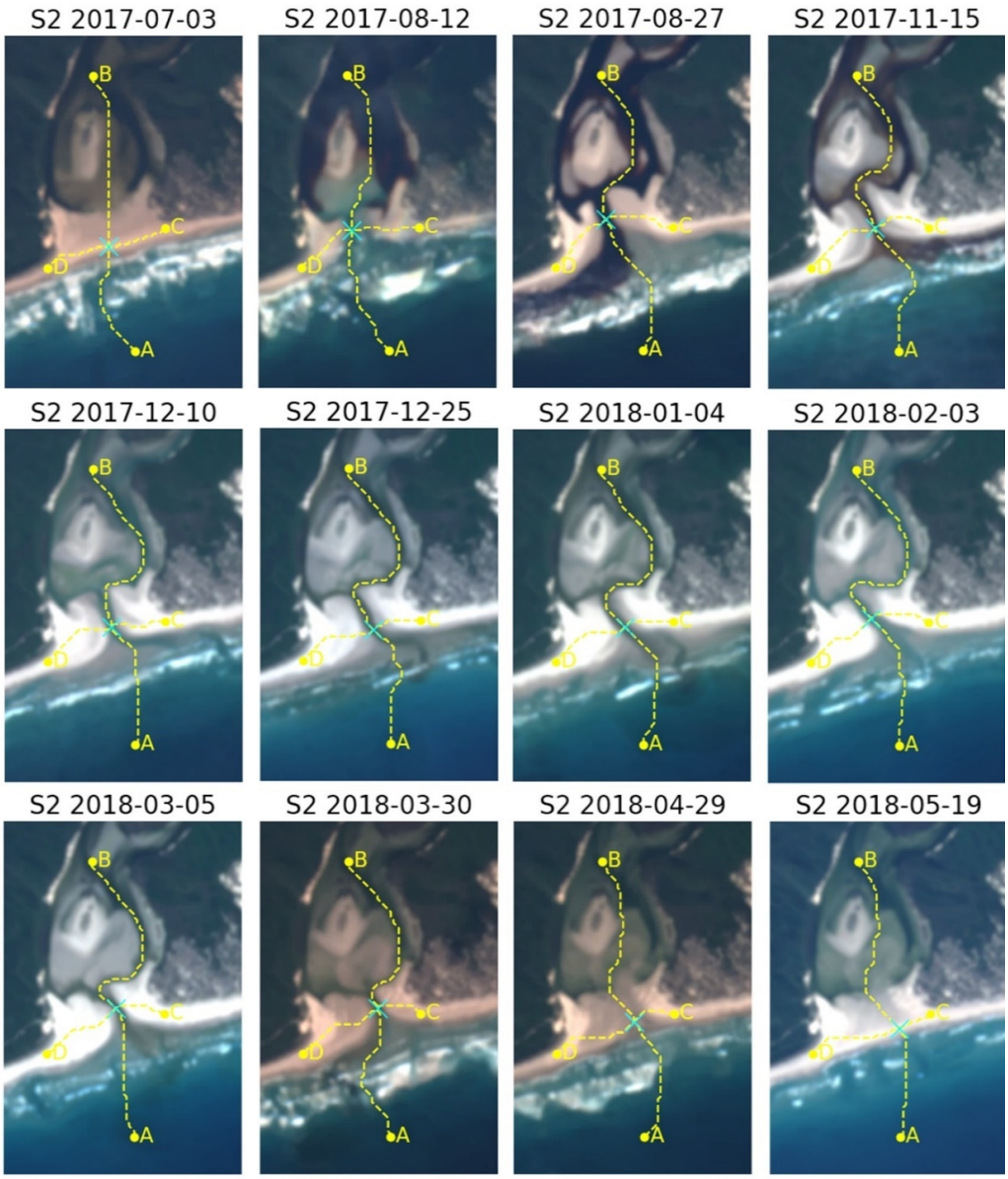


Figure 6: Least-cost pathfinding results for Inman River based on the S2 NIR band (10m resolution) through an approximately 8-month opening starting in August 2017. The automatically traced across-berm (A to B) and along-berm (C to D) (yellow lines) paths and their intersection (light blue cross) are overlaid on the true color S2 image from which they are derived. The across-berm path consistently identifies the on average deepest connection between points A and B.

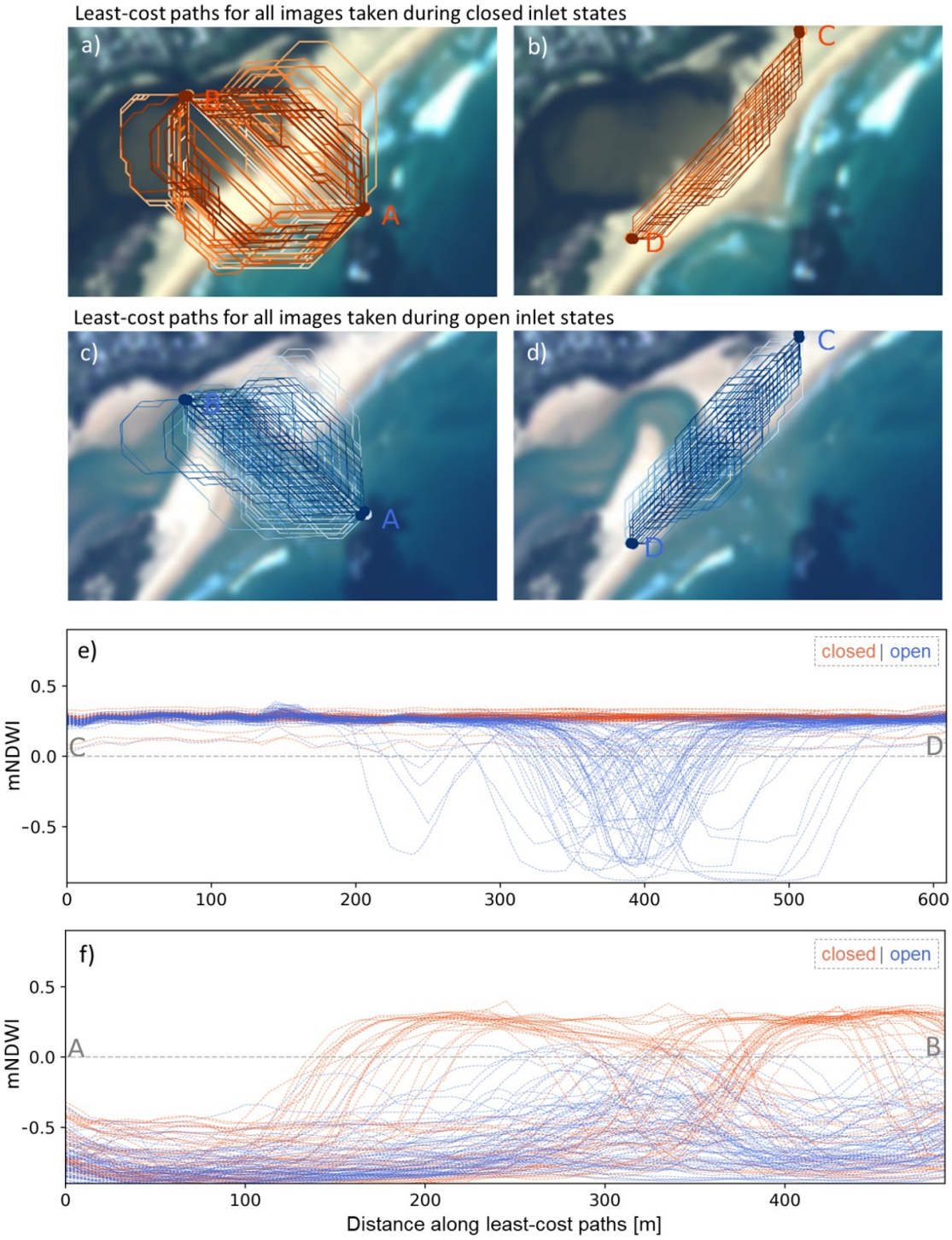


Figure 7: Results of the least-cost pathfinding algorithm for Durras and S2 imagery only (2016-2020). Across-berm (a) and along-berm (b) transects during closed inlet states overlaid on an example RGB S2 image. Across-berm (c) and along-berm (d) transects during open inlet states. Panel (e) shows the mNDWI extracted along all of the along-berm paths shown in panels (b) and (d). Panel (f) shows mNDWI extracted along the across-berm paths of panels (a) and (c).

### 3.2 Reconstructing inlet states over the full satellite record (1987-2020)

After confirming the ability of InletTracker to accurately trace openings, we applied it to reconstruct historic inlet dynamics for all 12 test sites and compared those results against the three validation datasets. Figure 8 shows time series of the along-berm Δ-to-median parameter over the full satellite record for the four focus sites. Also shown are the observational inlet state record (DPIE, 2020a), the visually inferred inlet states, and the tidal attenuation inferred from the in-situ water levels (DPIE, 2020b). The number of sufficiently cloud-free images with visually inferred open or closed inlets available for each site was 642 for Durras, 548 for Conjola, 676 for Coila and 489 for Wamberal (Table 2). The observational inlet states illustrate the dramatically different inlet dynamics of the four inlets, with Durras and Conjola exhibiting openings that can last for several years at a time, while Coila and Wamberal stay open for a couple of months or weeks at a time, respectively. Of the four inlets, Wamberal has by far the most dynamic inlet with several short openings per year, many of which are due to manual opening of the inlet channel (Gladstone et al., 2006).

When comparing the Δ-to-median parameter against the visually inferred binary inlet states for Durras and Conjola (Figure 8a and b), it can be seen that the parameter provides a good indicator of the state of the inlet. During openings, it tends to vary significantly around a site-specific mean value of between 0.4 to 1, which is likely due to variations in the tide and changes in the shape of the channel. During closed inlet states, the parameter consistently approaches zero. For some of the major openings in Conjola (e.g., 1994, 2018) and, to a lesser extent for Durras (1994, 2003), it appears that the parameter gradually decreases towards the end of open periods, as the inlet starts accumulating marine sediments, before closing entirely. The tidal attenuation records support this observation, with the lowest attenuation often occurring right after the inlet is flushed open, before gradually increasing back towards 100% attenuation during the inlet closure process (e.g., see openings starting in 2003, 2005 and 2007 in Durras).

For Durras and Conjola, there is very good agreement between the Δ-to-median parameter and the visually inferred inlet states, the observational record and the degree of tidal attenuation. In fact, for

Durras, an almost perfect result is obtained, with very good agreement between all parameters, except for the period around 2013 to 2015. In this period, both the Δ-to-median parameter and the tidal attenuation are reflective of an open inlet, indicating that there is likely a gap or error in the observational record. For Conjola, there is also very good agreement between all datasets for most of the time, except for the presumably wrong indicated inlet state in the observational record between 1999 and 2012. Notably, the relatively fast alternations between open and closed inlet states between 1995 and 1998 in Conjola are reasonably well captured by the Δ-to-median parameter.

Due to their much smaller and shallower inlet channels, the Δ-to-median parameter is much lower for Coila and Wamberal during open inlet states (Figure 8c and d) and the class separation between open and closed is less pronounced. For Coila, comparison of all parameters shows that not all the short inlet openings indicated in the observational record are detected by the Δ-to-median parameter or the visually inferred inlet states (e.g., see openings between 2003 and 2015). Nevertheless, several other openings such as those in the 80s, 90s and post 2015s are captured well.

For Wamberal, the reduced number of available images combined with the higher frequency and shorter duration of openings highlight the limitations of InletTracker, both in the spatial and temporal domain. Although some of the openings are accompanied by markedly higher Δ-to-median values and visually inferred open inlet states, most openings indicated in the observational inlet record remain undetected. These undetected openings are either the result of no cloud free images coinciding with an opening, or a lack of signal in the Δ-to-median parameter.

Since the beginning of the S2 record in mid-2015, there is a notable increase in the sampling frequency for all sites. The considerably higher spatial resolution of the S2 imagery also means that inlet openings are better resolved and, in particular for Wamberal, this appears to lead to significantly better detection of openings, both visually and via InletTracker.

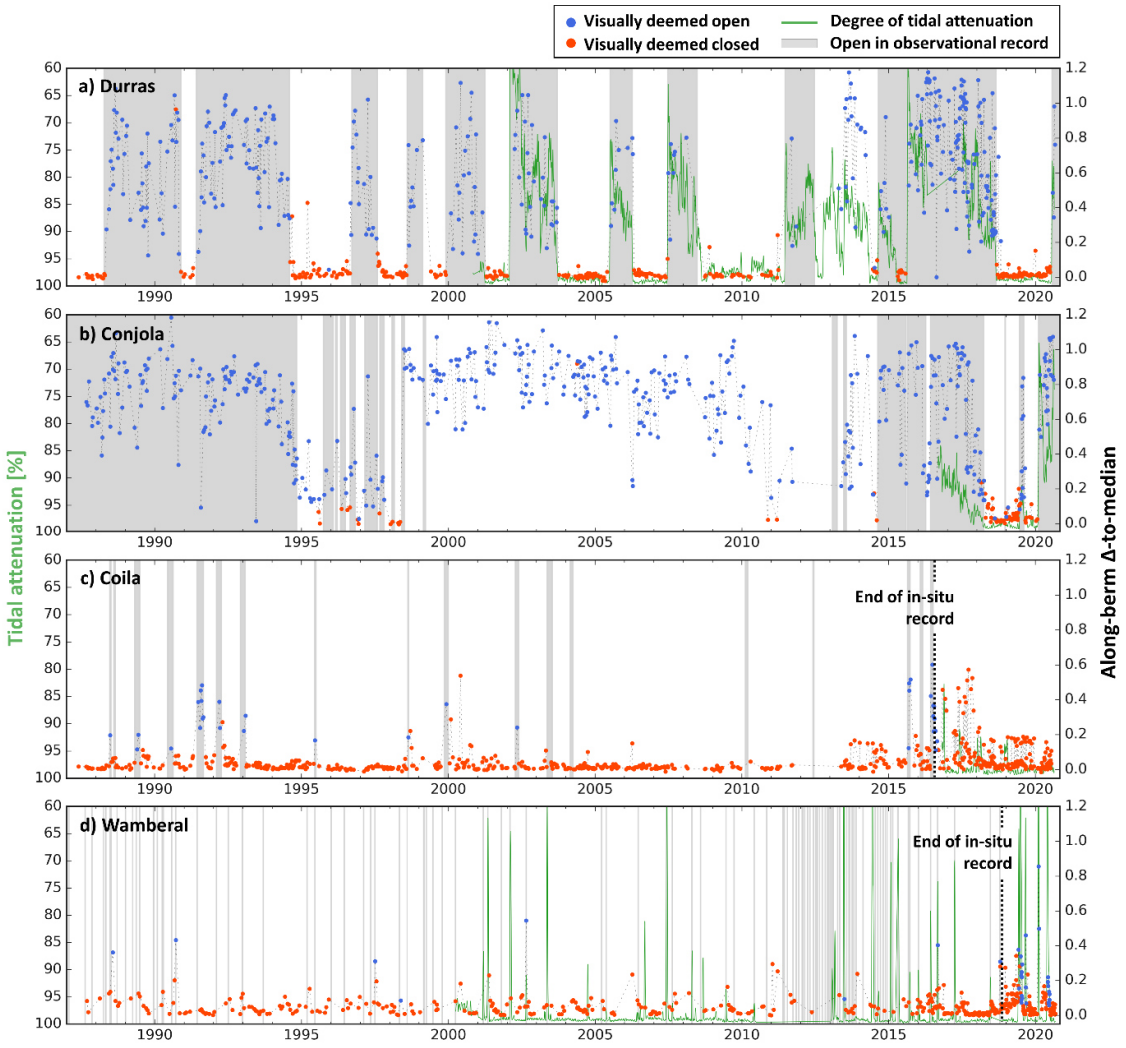


**Figure 8:** Time series of Δ-to-median values derived from the along-berm transect of each image for Durras, Conjola, Coila and Wamberal for the full L5, 7, 8 and S2 record. Pathfinding was based on the SWIR1 band, while the Δ-to-median was calculated based on the mNDWI. The degree of tidal attenuation derived from in-situ water levels (DPIE, 2020b) is shown in green. Grey background shading represents open inlet states as indicated in the observational records (DPIE, 2020a). The end of the observational records is indicated for Coila and Wamberal.

By and large, the above visual observations regarding the skill and limitations of InletTracker are confirmed by the accuracy assessment of the binary classification (Table 2). The total number of cloud free images (excluding all images deemed 'unclear') available for each site varied from a maximum of 642 for Durras, to a minimum of 162 for Irwin Inlet and averaged 411. Hamersley Inlet, Stokes Inlet

and Irwin inlet are located in Southwestern Australia and the low number of images here is the combined result of reduced sampling via the S2 satellites and persistent issues with the Landsat cloud mask over bright sand areas. Averages of 299 images during closed inlet states vs. 112 images during open inlet states across all sites indicate that most test sites are predominantly closed, which is in good agreement with the Inlet Closure Indices provided in Table 1. Inlets that appear to be predominantly open include Durras, Conjola and Irwin inlet. In contrast, Hamersley Inlet and Stokes Inlet were only open on 7 and 6 images, respectively, over the satellite record.

On average across all sites, InletTracker achieved an accuracy of 0.89 and 0.7 for predicting binary inlet states based on across-berm and along-berm pathfinding, respectively. F1-scores are more indicative of the performance of the algorithm in correctly detecting open inlet states and were 0.64 and 0.52 for the across-berm and along-berm classifications. These results indicate that, on average, the across-berm approach outperforms the along-berm approach for inlet state detection, although sites such as Narrabeen and Conjola showed slightly better performance for the along-berm approach. Very good results were obtained for larger inlets including Coila (accuracy=0.99; F1-score=0.86), Durras (accuracy=0.98; F1-score=0.99), Conjola (accuracy=0.97; F1-score=0.98) and Irwin inlet (accuracy=0.96; F1-score=0.97). Nadgee, Dee Why and Stokes inlet showed good accuracies but low F1-scores, which can be partially attributed to their relatively small number of actual positives (i.e., images during open inlet states), where even a small number of false positives or false negatives can lead to poor F1-scores.

As expected, algorithm performance is also strongly dependent on the size of inlet openings, with the two smallest sites Inman River and Curl Curl showing poor results. The relatively high across-berm accuracy obtained for these sites is the result of the low number of images during open inlets. Although the across-berm $\Delta$-to-median series for Inman River and Curl Curl are noisy and without clear class separation (not shown), classification thresholds of 0.01 and 0.19, respectively, placed the majority of images in the closed category for both sites, leading to high accuracy values (i.e.,

overfitting). The corresponding F1-scores of 0.19 and 0.25 provide a better indication of the poor algorithm performance for these sites.

**Table 2:** Validation statistics obtained via comparison of algorithm results against visually inferred inlet states for the full L5,7,8 and S2 imagery record. Accuracy metrics are provided separately for the across-berm (A to B) and along-berm (C to D) approach. The total number of images that were visually classified into open vs. closed inlet states and the number of images for each class is also provided. The optimal classification threshold was used to classify images into open vs. closed states based on the Δ-to-median parameter, where Δ-to-median > threshold = open.

| Inlet site | Transect direction | F1-score | Accu-racy | True neg. | False pos. | False neg. | True pos. | Classification threshold | Total nr. Of images | Nr. Of closed images | Nr. Of open images |
|---|---|---|---|---|---|---|---|---|---|---|---|
| Inman River | A-B | 0.19 | 0.79 | 307 | 33 | 50 | 10 | 0.01 | 400 | 340 | 60 |
| | C-D | 0.30 | 0.33 | 73 | 267 | 2 | 58 | 0.03 | - | - | - |
| Curl Curl | A-B | 0.25 | 0.89 | 396 | 21 | 28 | 8 | 0.19 | 453 | 417 | 36 |
| | C-D | 0.19 | 0.43 | 163 | 254 | 6 | 30 | 0.12 | - | - | - |
| Dee Why | A-B | 0.59 | 0.86 | 322 | 30 | 29 | 43 | 0.08 | 424 | 352 | 72 |
| | C-D | 0.68 | 0.88 | 324 | 28 | 21 | 51 | 0.11 | - | - | - |
| Coila | A-B | 0.86 | 0.99 | 640 | 3 | 6 | 27 | 0.11 | 676 | 643 | 33 |
| | C-D | 0.63 | 0.95 | 619 | 24 | 7 | 26 | 0.19 | - | - | - |
| Wamberal | A-B | 0.47 | 0.94 | 444 | 12 | 19 | 14 | 0.16 | 489 | 456 | 33 |
| | C-D | 0.54 | 0.94 | 443 | 13 | 16 | 17 | 0.19 | - | - | - |
| Narrabeen | A-B | 0.62 | 0.52 | 35 | 92 | 32 | 100 | 0.01 | 259 | 127 | 132 |
| | C-D | 0.74 | 0.67 | 48 | 79 | 7 | 125 | 0.07 | - | - | - |
| Nadgee | A-B | 0.46 | 0.91 | 371 | 32 | 5 | 16 | 0.19 | 424 | 403 | 21 |
| | C-D | 0.12 | 0.34 | 123 | 280 | 1 | 20 | 0.19 | - | - | - |
| Hamersley Inlet | A-B | 0.67 | 0.98 | 205 | 3 | 2 | 5 | 0.08 | 215 | 208 | 7 |
| | C-D | 0.54 | 0.94 | 196 | 12 | 0 | 7 | 0.15 | - | - | - |
| Conjola | A-B | 0.96 | 0.93 | 47 | 26 | 11 | 464 | 0.07 | 548 | 73 | 475 |
| | C-D | 0.98 | 0.97 | 66 | 7 | 9 | 466 | 0.12 | - | - | - |
| Durras | A-B | 0.99 | 0.98 | 269 | 6 | 5 | 362 | 0.1 | 642 | 275 | 367 |
| | C-D | 0.99 | 0.98 | 268 | 7 | 3 | 364 | 0.11 | - | - | - |
| Stokes Inlet | A-B | 0.63 | 0.98 | 230 | 5 | 1 | 5 | 0.16 | 241 | 235 | 6 |
| | C-D | 0.12 | 0.68 | 160 | 75 | 1 | 5 | 0.19 | - | - | - |
| Irwin inlet | A-B | 0.97 | 0.96 | 53 | 3 | 4 | 102 | 0.1 | 162 | 56 | 106 |
| | C-D | 0.44 | 0.29 | 1 | 55 | 60 | 46 | 0.01 | - | - | - |
| Average | A-B | 0.64 | 0.89 | - | - | - | - | 0.11 | 411 | 299 | 112 |
| Average | C-D | 0.52 | 0.70 | - | - | - | - | 0.12 | - | - | - |

Lastly, this experiment provides some insights into the optimal threshold for classifying the Δ-to-median series into binary inlet states. A higher threshold will place more images in the closed category and vice versa. The average across-berm and along-berm- thresholds that lead to the highest

F1-scores are 0.11 and 0.12, respectively, and, for the best performing sites, the optimal threshold is commonly very close to 0.1 (i.e., 0.07-0.12).

### 3.3 High resolution monitoring of inlet dynamics via Sentinel-2 only (2016-2020)

This section provides InletTracker results for S2 imagery only (NIR/NDWI configuration), to illustrate that the underlying 10m resolution and up to 5-day sampling frequency considerably improves the skill of the algorithm for detecting smaller and shorter duration openings. Figure 9 shows the corresponding time series of the along-berm Δ-to-median parameter along with the three validation datasets for the four focus sites. The corresponding accuracy metrics for all 12 test sites are provided in Section S2 of the Supplementary Materials.

For the four focus sites, InletTracker showed excellent performance with F1-scores and accuracies of 0.98 and 0.98 for Durras, 0.94 and 0.95 for Conjola, 1.0 and 1.0 for Coila, and 0.89 and 0.98 for Wamberal. The time series plots in Figure 9 reflect this good performance, showing a distinct class separation in the Δ-to-median parameter for open vs. closed inlet states. In fact, for Durras and Conjola, InletTracker appears to outperform the human analyst as indicated by several images wrongfully inferred as open despite the Δ-to-median parameter and the other two validation datasets clearly indicating a closed inlet (e.g., late 2018, early 2019 for Conjola). Even though Coila and Wamberal show equally good class separation in the Δ-to-median parameter, and near perfect agreement with the visually inferred inlet states, one of the openings of Coila and several openings of Wamberal are missed entirely due to a lack of coinciding images. Thanks to the very high sampling frequency of S2-A and B from around 2018 and onwards, however, this represents less of an issue in more recent times. Importantly, the S2 acquisition frequency is not uniform around the globe and can therefore vary substantially for different inlets (see Bergsma and Almar (2020) for global coastline sampling frequencies).

Across the 12 test inlets, excellent average F1-scores and accuracies of 0.79 and 0.94 for the along-berm and 0.75 and 0.91 for the across-berm predictions were obtained. Similar to the results of the full

imagery record, the lowest performance was obtained for small sites such as Inman River, Dee Why and Curl Curl, which suffer from elevated numbers of false positives and false negatives.

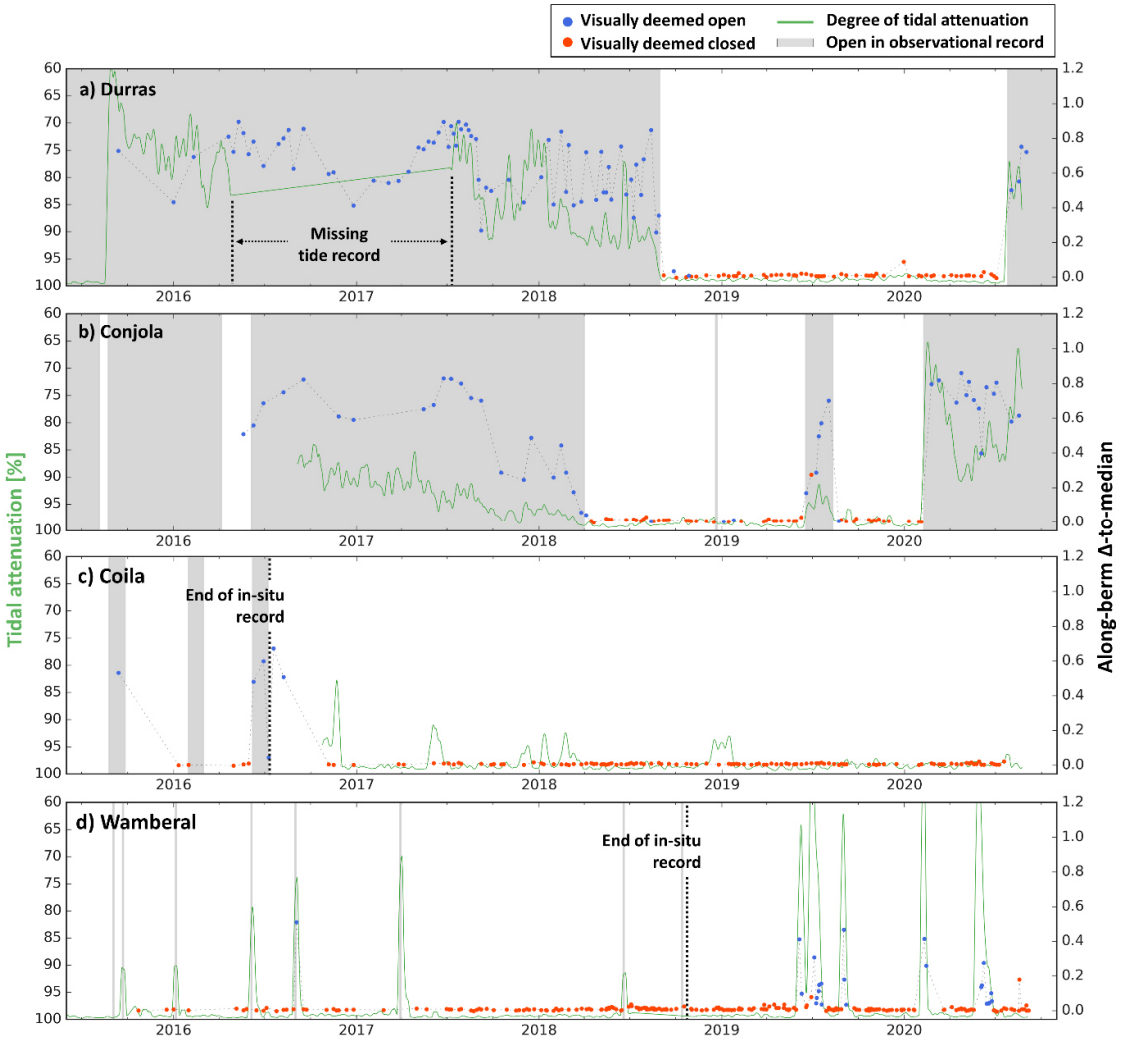


**Figure 9:** InletTracker results for S2 only in the 10m resolution NIR/NDWI configuration showing time series of Δ-to-median values derived from the along-berm transect of each image for Durras, Conjola, Coila and Wamberal.

### 3.4 Correlation between Δ-to-median and tidal attenuation

To test whether the Δ-to-median variable can provide an approximation of the degree of opening of an inlet, the S2-based along-berm Δ-to-median series was compared against the degree of tidal attenuation for seven sites for which in-situ water level records date back to at least 2015. The results

indicate that there is a degree of correlation between the two parameters for some sites, even without adjusting the Δ-to-median parameter for the tide level at the time of image capture (Table 4). For Dee Why, Wamberal, Durras and Conjola, negative statistically-significant ($p<0.05$) Pearson correlations of below -0.7 were obtained. For Curl Curl and Coila, weak correlations were found, while Narrabeen was roughly between these and the better performing sites.

**Table 4:** Validation statistics (Pearson correlation and corresponding p-value) obtained via comparison of the along-berm (C-D) Δ-to-median parameter against tidal attenuation for seven sites for which in-situ water level data inside the inlet was available for the full S2 imagery record (DPIE, 2020b).

| Site | Pearson correlation | p-value of Pearson correlation |
|---|---|---|
| Curl Curl | -0.31 | 0.000023 |
| Dee Why | -0.72 | 0.000000 |
| Wamberal | -0.74 | 0.000000 |
| Narrabeen | -0.62 | 0.000000 |
| Coila | 0.14 | 0.135293 |
| Durras | -0.89 | 0.000000 |
| Conjola | -0.76 | 0.000000 |

### 3.4 The effect of tide on algorithm performance

The harmonic oscillations in water levels in open inlet channels created by the tide (e.g., Figure 5) represent one of the core challenges for automated detection of inlet states through multi-temporal imagery. Even without any geomorphic change, the appearance and reflectance spectra of an inlet can change dramatically depending on the tide level at the time of image capture. To illustrate, we selected two S2 images that were taken 5-days apart and during alternating states of the tide (Figure 10). On the true color images, the difference in water level of approximately 1.1m between the two scenes is clearly visible, with several of the shallow sand bar features on either side of the inlet being barely visible on the high tide image. The difference in water level also affects the subsequent pathfinding and transect analysis steps. Despite nearly identical channel geometries, across-berm pathfinding resulted in a more direct connection between the seed and receiver points for the high

tide image. This is the result of the additional 1.1m of water column dramatically reducing the cost over shallow sand bar features. Although the location of the along-berm paths was nearly identical for both images, the increased water level of the high tide image is strongly reflected in the corresponding NDWI transects, which depicts a substantially wider and deeper response over the channel during high tide.

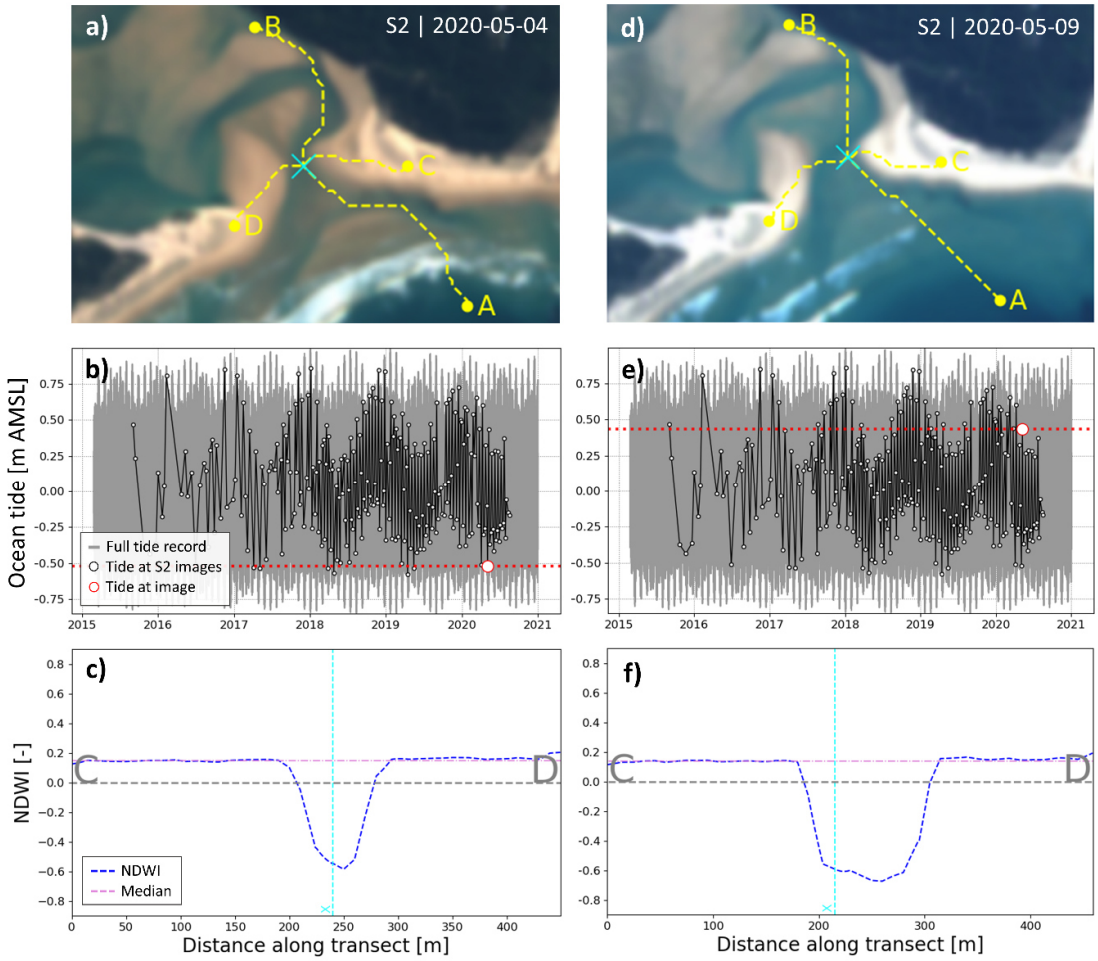


**Figure 10:** Effects of tide on InletTracker results showing (a) true color S2 image taken on 04.05.2020 at a lower tide ($z_{tide}$ = -0.5 m above mean sea level); (b) time series of the local ocean tide water level overlaid by tide water levels of all available S2 images (white dots); (c) along-berm (C to D) NDWI transect and median of the transect for the same image. (d), (e) and (f) show the same as (a), (b) and (c) but for an S2 image from the 09.05.2020, when the tide was relatively high ($z_{tide}$ = 0.6 m above mean sea level). The effects of the approximately 1.1m difference in tide on water depth in the inlet channel and corresponding NDWI transects is clearly visible when comparing panels (c) and (f). Tide levels are obtained from the FES global tide model (Lyard et al., 2020).

This sensitivity test confirms that the state of the tide has substantial influence on the location of least-cost paths and corresponding NDWI or mNDWI transects. For instance, for small inlets or inlet channels that have accumulated enough sediment to approach closure, the state of the tide alone could determine whether the algorithm predicts an open or closed inlet state (also see discussion on transitional inlet states in section 4.3). Similarly, the state of the tide would also strongly affect any estimation of the width and depth of an inlet channel (see discussion in section 4.6). To address these issues, InletTracker integrates the FES global tide model (Lyard et al., 2020) to identify the state of the tide during the time of image capture (e.g., Figure 10b and e), a method that is extensively documented and tested as part of Vos et al. (2020). Although there is currently no tide correction routine implemented for the Δ-to-median parameter, this enables users to filter the imagery record for specific tidal levels or to exclude images taken during very high or low tides from the analysis.

## 4. Discussion

The state and dynamics of an inlet has a profound impact on the eco-hydrological character and functioning of inlets, but often remains poorly and inconsistently quantified. Here, we introduced InletTracker, a GEE-enabled open-source python toolkit for tracking the time-evolving state of dynamic coastal inlets. InletTracker uses a simple but effective pathfinding and transect analysis approach that leverages the information content of the satellite imagery to a high degree. One of the key benefits of InletTracker is that it can reconstruct the dynamics of inlets from 1986 to present with only minimal user input for setup and calibration. Further, due to its open-source and user-friendly nature, along with its GEE-facilitated image acquisition and pre-processing routine, it is also easily applicable to other inlets around the world. In the following sections, we discuss the current performance of InletTracker, opportunities for expanding its capabilities in the future and potential applications around the world.

### 4.1 Algorithm performance

The first key step of the InletTracker method, namely the tracing of the inlet channel along and across the berm through the shallowest and deepest part, respectively, showed excellent performance. The only other application of a least-cost pathfinding algorithm in a related context is that of Chen et al. (2020), who used this approach to identify river centrelines, albeit not from band or spectral indices that are proportional to water depth. Further, with an average accuracy of 0.89 (across-berm) and 0.94 (along-berm) across the 12 test sites for all satellites and S2 only, respectively, InletTracker also performed very well in predicting binary inlet states. These statistics are based on a total of 6363 unique binary inlet state predictions. As anticipated, performance is linked to the size of inlets, with the algorithm achieving near perfect results for the four largest inlets, while performing poorly for the smallest tested inlets, in particular for those that exhibit frequent short duration openings. The limited performance for smaller sites is partially overcome when using S2 in the NIR/NDWI configuration, which increases the performance in the spatial domain (i.e., in terms of the tool being able to detect inlet states more accurately for small sites). Overall, the comparison against the observational record (DPIE, 2020a) and the degree of tidal attenuation (DPIE, 2020b) revealed very similar performance patterns. For instance, for the four focus sites, the visually inferred inlet states, observational record, and degree of tidal attenuation depict nearly identical sequences of open vs. closed inlet states (e.g., Figure 9). These sequences are mostly mimicked well by the Δ-to-median parameter for S2, which alternates between its two distinct modes for open vs. closed inlet states. This strong agreement across the three independent validations indicates that the binary classification accuracy metrics provided in Tables 2 and S1 provide a robust and accurate picture of the performance of InletTracker across the 12 test sites. Our experiments also show that the Δ-to-median is, to some extent, correlated to the degree of inlet opening. Despite the noise in the Δ-to-median parameter resulting from the tide, statistically significant correlations of -0.7 were found between the Δ-to-median parameter and the degree of tidal attenuation for four of the seven inlets that were tested in this regard. These findings suggest that the

Δ-to-median parameter can be useful for monitoring and predicting the closure of an inlet if the tide is carefully accounted for and further investigation of this pathway is encouraged.

### 4.2 Spatio-temporal resolution constraints

Some of the key performance limitations of InletTracker are the result of inherent physical limitations of the satellite data, rather than the algorithm itself. The spatio-temporal resolution constraints associated with the mapping of surface water dynamics based on the Landsat record with its ≥16 days revisit and 30m resolution are discussed in detail in Heimhuber et al. (2018). Due to these inherent features of the Landsat record, small inlet openings are often not sufficiently resolved by the imagery to provide enough signal for accurately inferring the state of an inlet. The magnitude of this signal strongly depends on the location, size, and depth of the inlet channel and its location in relation to the pixel(s) covering this part of an image. In summary, increasingly small (open) inlet channels lead to increasingly weak and mixed spectral signals for the pixel(s) covering these channels, resulting in increasingly poor inlet state detection accuracy. Although not explicitly tested here, we estimate that the algorithm starts to reach its limits when the width of an inlet channel is lower than the width of a pixel in the respective input imagery (i.e., 30m for Landsat, 10m for S2).

Accordingly, the satellite revisit interval of 16 days under ideal conditions and multiples of 16 days in the presence of clouds means that openings which only last for several days or weeks are often not captured in the Landsat record (i.e., prior to 2016). This effect is not captured by the accuracy metrics of Tables 2 and S1, since those are based on inlet states visually inferred from the imagery itself. However, comparison against the observational inlet state records and the degree of tidal attenuation provided insights into the nature of this problem (i.e., Figures 8 and 9). The comparison showed that for sites such as Wamberal, short openings of the highly dynamic inlet are often missed throughout the Landsat record. Due to increased temporal (i.e., ≥ 5-daily) and spatial (i.e., 10m) sampling provided by S2 (Rott et al., 2012), as well as the overlap between S2 and L8, these spatio-temporal

resolution constraints are considerably less problematic for applications concerned with inlet dynamics after 2016.

### 4.3 Dealing with transitional inlet states

One of the challenges of classifying inlets into open vs. closed (i.e., binary) states is that ambiguity arises during the transitional period before an inlet closes fully. At this point in time, an inlet berm may have recovered sufficiently to inhibit most tidal exchange but, at the same time, over wash and shallow inundation can still occur in the inlet during high tides, storm surges or large swells (e.g., see S2 image from 29-04-2018 in Figure 6). Whether such a transitional inlet state is best described as closed or open depends on the analysis and/or goal of a particular application but, more importantly, this creates a problem for automated detection of inlet states. Such transitional inlet states typically lead to Δ-to-median values close to the optimal classification threshold, resulting in a rather arbitrary classification as either open or closed. For some applications, it might therefore be advantageous to work directly with the Δ-to-median parameter as an inlet state indicator instead of binary inlet states. This way, a gradual decrease in the Δ-to-median parameter towards zero at the end of an open period could provide some indication for when an inlet is about to close fully, which can be observed for Durras and Conjola in Figure 8, for example. The ambiguity surrounding transitional entrance state is likely also a key reason for the discrepancies between the single analyst visually inferred entrance states and the entrance states obtained via the majority vote of the six additional analysts.

### 4.4 Comparison with alternative methods

To the best of our knowledge, there is only one other study that reconstructed multidecadal inlet dynamics of an inlet (Nadgee) from satellite imagery (Scanes et al., 2020). By relating in-situ water levels with remotely sensed surface water areas (Mueller et al., 2016), which were then used to infer inlet openings, this approach essentially bypasses spatial resolution constraints associated with small inlets. The detection of inlet states post opening (infilling and eventual closure) was not attempted in this study but, due to limited correlation of the closure process with the estuary water body area, is

likely limited. Nevertheless, it does represent an elegant solution to the problem at hand and we encourage a direct comparison of this method against InletTracker.

Although not developed for the purpose of inlet state detection, a number of related algorithms have been shown to provide waterline locations with sub-pixel accuracy and as such, could potentially be applied in this context (Bishop-taylor et al., 2019; Bishop-Taylor et al., 2019; Sanchez-García et al., 2020; Vos et al., 2019a). Interestingly, Vos et al. (2019a) found no significant differences in the accuracies of shorelines obtained via Landsat and S2, despite the higher resolution of the latter. In contrary, we found considerably improved performance for small inlets when using S2 in the 10m resolution NIR and NDWI configuration. Ultimately, waterline or shoreline mapping differs from inlet state detection in that the former usually deal with a single curvilinear interface between two distinct and spatially large classes (i.e., ocean and beach). If confronted with an inlet channel that may have a width of approximately one pixel, it is likely that most of these algorithms would produce spurious results without a targeted expansion of the functionality.

Algorithms such as those behind RivaMap (Isikdogan et al., 2017) or the method of Gong et al. (2020) are specifically designed for mapping shallow channel networks and could potentially be useful for coastal inlets. Both approaches use sophisticated methods that either enhance the contrast between shallow channels and the surrounding landforms (Gong et al., 2020), or leverage the typically curvilinear shape of such channels via sophisticated image filtering techniques (Isikdogan et al., 2017). A major advantage of both methods over InletTracker is their ability to map entire river or delta channel networks, rather than a single selected inlet channel. The method of Gong et al. (2020) was validated on a few selected images and, to our best knowledge, does not provide an open-source software package. In contrast, RivaMap is an open-source python toolbox capable of mapping river channels on large spatio-temporal scales from Landsat imagery and we encourage a comparison of this tool against InletTracker.

### 4.5 Opportunities for inferring width and depth of inlet channels

Currently, InletTracker does not include functionality for identifying the width and depth of inlet channels. If desired, the width of the shallowest section of an inlet channel during a specific tide level could be inferred from the along-berm NDWI or mNDWI transect either using a suitable thresholding technique (e.g., Bishop-taylor et al. (2019); Vos et al. (2019a)), a specific along-berm percentile, or a more complex approach such as the inflection point method proposed by Sánchez-García et al. (2020). If the width of a channel at the bottleneck can be inferred accurately via this method for different levels of the tide but for images obtained close in time (i.e., as done for Figure 10), one could potentially reconstruct the shape of the inlet channel.

Regarding the depth of the channel, several studies have illustrated that shallow water bathymetry can be inferred from satellite imagery via targeted algorithms (Chybicki, 2017; Jiang, 2014; Misra and Ramakrishnan, 2020; Niroumand-jadidi et al., 2020; Poliyapram et al., 2017; Poursanidis et al., 2019; Siermann et al., 2014). This technique is commonly referred to as satellite derived bathymetry (SDB) and has previously been shown to yield satisfactory results for Landsat (Misra and Ramakrishnan, 2020) and S2 imagery (Chybicki, 2017; Poursanidis et al., 2019). Correspondingly, it should be possible to infer the water depth along the along-berm and across-berm transects via SDB. The band relationships commonly used in SDB are sensitive to several scene specific factors such as lighting and atmospheric conditions, sun glitter, the composition of water, and the spectral signature of the bottom. Consequently, SDB algorithms either require in-situ data for calibration (e.g., Chybicki (2017); Poliyapram et al. (2017)), or a set of spectral models that appropriately account for all of these factors (e.g., Ohlendorf et al. (2011)). It is due to these complexities that we did not include such functionality in InletTracker. The often-rapid changes in water composition and color due to inlet opening and closure dynamics (e.g., see Figure 6) and the daily oscillations of the tides (e.g., Figure 10) pose major challenges in this context.

### 4.6 Global application opportunities

To further illustrate the usefulness of InletTracker for inlet management and research around the world, we applied the publicly-available version of the tool to three coastal inlets that have undergone a significant opening or closure event between 1986 and now (Figure 11). For this test, we generated only minimal training data (i.e., 10 open and 10 closed inlet states) and manually rejected poor-quality images that were missed by the cloud cover filter. The mouth of the Rio Grande (Figure 11a), the fourth longest river in the U.S., is located in the Gulf of Mexico on the U.S.-Mexican border. Very high levels of water abstraction for irrigated agriculture and other water uses in its catchment have dramatically reduced flows in the Rio Grande, causing a 200km stretch of the river known as 'The Forgotton Reach' to occasionally dry out for long periods of time (Johns and VanNijnatten, 2021). As can be seen in the time series of across-berm Δ-to-median parameters, these high upstream abstraction levels contributed to the complete closure of the Rio Grande's river mouth from April to July 2001 and then again from November 2001 to November 2002, an event that remains poorly documented in the scientific literature.

Both the second and third examples provided in Figure 11b and c respectively are barrier island breaches. In August 2011, Hurricane Irene moved up the U.S. East Coast and lead to the creation of an initially roughly ~50m wide and 3.5m deep breach known as the Pea Island Breach in the Outer Banks of North Carolina (Velasquez Montoya et al., 2018). Despite the poor data coverage of 2012 owed to the ceasing of operation of Landsat 5 at the end of 2011 and the Landsat 7 scan line error post 2003, InletTracker was able to capture the opening of the breach in 2011, its initial closure in mid-2013 as well as its full closure at the end of 2013 (Figure 11b). Similarly, in October 2012, Hurricane Sandy made landfall over New Jersey, leading to the formation of the so-called Wilderness Breach on Fire Island on the southern side of Long Island (van Ormondt et al., 2020b). In contrary to the Pea Island Breach, the Wilderness Breach has remained permanently open as can be seen in the corresponding InletTracker results (Figure 11c). To illustrate the tool's ability to monitor the morphological evolution

of the breach, Figure 11c further shows the last across-berm path obtained for every year since the opening of the breach, which migrated about 100m in south-west direction over this period.

Although these two barrier breaches are well documented in the literature, these results illustrate the great potential of InletTracker for supporting inlet management and research around the world. For instance, for inlets that are already being monitored via regular on-ground surveys, InletTracker could be integrated as a complementary data source to reduce costs and/or to increase the sampling frequency. The erratic nature of intermittent coastal inlets poses a particular challenge for decision and policy makers and the additional long-term data obtained via InletTracker could help to establish more evidence-based management strategies for inlets around the world.

As another example, the pathfinding and transect analysis components of InletTracker will help to gain new insights into the long-term morpho-dynamics of inlets and drivers thereof (e.g., Figure 11c). Furthermore, InletTracker could be useful for analysis and monitoring of similar shallow water landforms such as delta, river or estuarine channel networks, tidal flats, sand spits, floodplains, levees or freshwater wetlands and we strongly encourage the exploration of these pathways. In rivers or river channel networks that exhibit rapid channel migration patterns, InletTracker should be able to consistently trace the deepest part of the channel between two points along the river, even if the channels undergo major morphological changes. This would represent a major advantage over most existing remote sensing tools for river planform mapping, which yield the geometric river centreline, rather than the hydraulic centreline along which most of the river flow is conveyed.

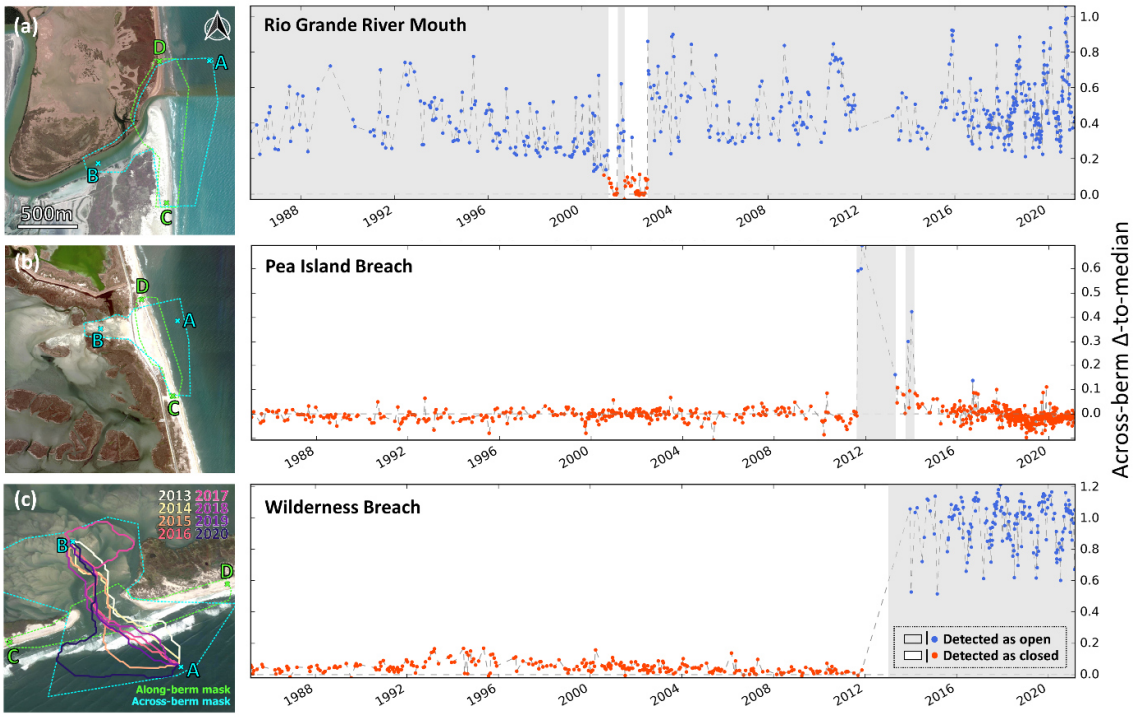


**Figure 11:** InletTracker results obtained with the public version of the tool and minimal user input for three selected coastal inlets with high socio-economic significance showing location and pathfinding configuration (left panels) along with the corresponding time series of the across-berm Δ-to-median parameter obtained via mNDWI-based pathfinding and transect analysis (right panels) for (a) the Rio Grande River mouth on the U.S.-Mexican border (-97.14742, 25.95590) in 2001; (b) the Pea Island Breach in the Outer Banks of North Carolina, U.S. (-75.48271, 35.68373); (c) the Wilderness Breach in Fire Island, New York, U.S. (-72.89806, 40.72386). For Wilderness Breach, the left panel also shows the last across-berm path of every year since the opening of the breach. Background imagery (Google Earth).

## 5. Conclusions

In this paper, a new tool for recent historic reconstruction (1986-present) and monitoring of inlet dynamics from publicly available satellite records was introduced. Apart from being limited by the spatio-temporal resolution constraints of the Landsat and S2 imagery records, our study highlighted that InletTracker is able to consistently and accurately infer open vs. closed inlet states and can even

provide an indication of the degree of inlet opening for larger inlets. Since the tool is provided free of charge as an open-source python software package, we envision for it to be used widely by coastal engineers, managers, and scientists for a range of applications. In coming months, we will apply InletTracker to generate a first quantification of inlet state dynamics over the past three decades for suitable intermittent inlets worldwide. The resulting dataset will help to answer a range of remaining questions around processes, dynamics, and drivers (i.e., waves vs. rainfall vs. tide) of inlets in different coastal and hydroclimatic settings around the globe. Ultimately, the dynamics of intermittent inlets are highly sensitive to changes in the climate and the state of their catchment (in the case of intermittent estuaries) and understanding changes in their long-term dynamics is critical for establishing suitable climate change adaptation and management strategies.

**Acknowledgements:** InletTracker uses some functionality associated with CoastSat and we thank its developer Kilian Vos for his involvement and guidance. We also thank Chris Leaman, Nashwan Matheen, Raimundo Ibaceta, Katrina Waddington and Matthew Shermot from the UNSW Water Research Laboratory for generating data for the accuracy assessment. We further thank the New South Wales Department of Primary Industries and the Environment (DPIE) for collecting and providing important datasets for this study.

**Conflicts of Interest:** The authors declare no conflict of interest.

**References**

Alluvium, 2012. Should it be open or closed ? Estuary management during prolonged periods of low catchment inflows and low water level conditions. Report P117019_R02 by Alluvium for the Corangamite Catchment Management Authority (CCMA) and the Department of Environment.

Baldock, T.E., Weir, F., Hughes, M.G., 2008. Morphodynamic evolution of a coastal lagoon entrance during swash overwash. Geomorphology 95, 398–411. https://doi.org/10.1016/j.geomorph.2007.07.001

Behrens, D.K., Bombardelli, F.A., Largier, J.L., Twohy, E., 2013. Episodic closure of the tidal inlet at the mouth of the Russian River - A small bar-built estuary in California. Geomorphology 189, 66–80. https://doi.org/10.1016/j.geomorph.2013.01.017

Bergsma, E.W.J., Almar, R., 2020. Coastal coverage of ESA' Sentinel 2 mission. Adv. Sp. Res. 65, 2636–2644. https://doi.org/10.1016/j.asr.2020.03.001

Bertin, X., Mendes, D., 2019. The Closure of a Shallow Tidal Inlet Promoted by Infragravity Waves 0–6. https://doi.org/10.1029/2019GL083527

Bishop-taylor, R., Sagar, S., Lymburner, L., Alam, I., Sixsmith, J., 2019. Sub-Pixel Waterline Extraction : Characterising Accuracy and Sensitivity to Indices and Spectra. Remote Sens. 2019, 11, 2984. https://doi.org/10.3390/rs11242984

Bishop-Taylor, R., Sagar, S., Lymburner, L., Beaman, R.J., 2019. Between the tides: Modelling the elevation of Australia's exposed intertidal zone at continental scale. Estuar. Coast. Shelf Sci. 223, 115–128. https://doi.org/10.1016/j.ecss.2019.03.006

Carmichael, V., 2000. An assessment of water resources and recharge in the Hindmarsh River, Inman River and Currency creek catchments. Thesis. http://hdl.handle.net/2440/103166

Chen, H., Liang, Q., Liang, Z., Liu, Y., Ren, T., 2020. Extraction of connected river networks from multi-temporal remote sensing imagery using a path tracking technique. Remote Sens. Environ. 246, 111868. https://doi.org/10.1016/j.rse.2020.111868

Chuwen, B.M., Hoeksema, S.D., Potter, I.C., 2009. The divergent environmental characteristics of permanently-open, seasonally-open and normally-closed estuaries of south-western Australia. Estuar. Coast. Shelf Sci. 85, 12–21. https://doi.org/10.1016/j.ecss.2009.03.030

Chybicki, A., 2017. Mapping South Baltic Near-Shore Bathymetry Using Sentinel-2 Observations. Polish Marit. Res. 24, 15–25. https://doi.org/10.1515/pomr-2017-0086

Department of Water, Government of Western Australia, 2007. Stokes Inlet Condition Statement. Available at: http://www.rivercare.southcoastwa.org.au/infodata/youngc/stokesi/benwenerup/condition.pdf; last accessed: 12.03.2021

DPIE, 2020a. NSW Department of Primary Industries and the Environment. In-situ records of ICOLL entrance openings.

DPIE, 2020b. NSW Coastal Data Network Program managed by the Climate Change and Sustainability Division of the Department of Planning, Industry and Environment (CCSD). Available at: https://mhl.nsw.gov.au/Data-Level, last accessed 12th of January, 2020.

Duong, T.M., Ranasinghe, R., Luijendijk, A., Walstra, D., 2017. Assessing climate change impacts on the stability of small tidal inlets : Part 1 - Data poor environments. Mar. Geol. 390, 331–346. https://doi.org/10.1016/j.margeo.2017.05.008

Duong, T.M., Ranasinghe, R., Thatcher, M., Mahanama, S., Wang, Z.B., Dissanayake, P.K., Hemer, M., Luijendijk, A., Bamunawala, J., Roelvink, D., Walstra, D., 2018. Assessing climate change impacts on the stability of small tidal inlets: Part 2 - Data rich environments. Mar. Geol. 395, 65–81. https://doi.org/10.1016/j.margeo.2017.09.007

Duong, T.M., Ranasinghe, R., Walstra, D., Roelvink, D., 2016. Assessing climate change impacts on the stability of small tidal inlet systems: Why and how? Earth-Science Rev. 154, 369–380. https://doi.org/10.1016/j.earscirev.2015.12.001

Gale, E.J., Pattiaratchi, C., Ranasinghe, R., 2007. Processes driving circulation, exchange and flushing within intermittently closing and opening lakes and lagoons. Mar. Freshw. Res. 58, 709–719.

https://doi.org/10.1071/mf06121

Gladstone, W., Hacking, N., Owen, V., 2006. Effects of artificial openings of intermittently opening estuaries on macroinvertebrate assemblages of the entrance barrier 67, 708–720. https://doi.org/10.1016/j.ecss.2006.01.008

Gong, Z., Wang, Q., Guan, H., Zhou, D., Zhang, L., Wang, X., Li, Z., 2020. Extracting tidal creek features in a heterogeneous background using Sentinel-2 imagery: a case study in the Yellow River Delta, China. Int. J. Remote Sens. 41, 3653–3676. https://doi.org/10.1080/01431161.2019.1707898

González-Villanueva, R., Pérez-Arlucea, M., Costas, S., 2017. Lagoon water-level oscillations driven by rainfall and wave climate. Coast. Eng. 130, 34–45. https://doi.org/10.1016/j.coastaleng.2017.09.013

Gordon, A., Nielsen, A., 2020. Large scale impacts of jetties and training walls – experience on the Australian East Coast, in: Coastal Engineering Proceedings, (36v), Structures.2. https://doi.org/https://doi.org/10.9753/icce.v36v.structures.2

Gorelick, N., Hancher, M., Dixon, M., Ilyushchenko, S., Thau, D., Moore, R., 2017. Google Earth Engine: Planetary-scale geospatial analysis for everyone. Remote Sens. Environ. https://doi.org/10.1016/j.rse.2017.06.031

Haines, P., 2006. Physical and chemical behaviour and management of Intermittently Closed and Open Lakes and Lagoons (ICOLLs ). NSW Griffith Centre for Coastal Management School of Environmental and Applied Sciences. Doctoral thesis.

Haines, P.E., Tomlinson, R.B., Thom, B.G., 2006. Morphometric assessment of intermittently open / closed coastal lagoons in New South Wales , Australia. Estuar. Coast. Shelf Sci. 67, 321–332. https://doi.org/10.1016/j.ecss.2005.12.001

Harley, M.D., Turner, I.L., Short, A.D., Ranasinghe, R., 2011. Assessment and integration of conventional , RTK-GPS and image-derived beach survey methods for daily to decadal coastal monitoring. Coast. Eng. 58, 194–205. https://doi.org/10.1016/j.coastaleng.2010.09.006

Hayes, M.O., FitzGerald, D.M., 2013. Origin, Evolution, and Classification of Tidal Inlets. J. Coast. Res.

14–33. https://doi.org/10.2112/SI

Heimhuber, V., Tulbure, M.G., Broich, M., 2018. Addressing spatio-temporal resolution constraints in Landsat and MODIS-based mapping of large-scale floodplain inundation dynamics. Remote Sens. Environ. 211, 307–320. https://doi.org/10.1016/j.rse.2018.04.016

[Dataset] Heimhuber, V., Vos, K., Glamore, W., 2021. InletTracker - A python toolkit for monitoring coastal inlets via Landsat and Sentinel-2, Mendeley Data, V2. https://doi.org/10.17632/10.17632/z9rywmv886.2

Isikdogan, F., Bovik, A., Passalacqua, P., 2017. RivaMap : An automated river analysis and mapping engine. Remote Sens. Environ. 202, 88–97. https://doi.org/10.1016/j.rse.2017.03.044

Isikdogan, F., Bovik, A., Passalacqua, P., 2015. Automatic Channel Network Extraction From Remotely Sensed Images by Singularity Analysis. IEEE Geosci. Remote Sens. Lett. 12, 2218–2221, doi: 10.1109/LGRS.2015.2458898.

Jiang, C.Y.H., 2014. Bottom-up Bathymetric Modeling in Investigating Quality and Quantity of Highly Polluted Water in Large Scale Inland Lake Using Remote Sensing Imagery and Digital Elevation Model. Am. J. Environ. Eng. 4, 117–141. https://doi.org/10.5923/j.ajee.20140405.05

Johns, C., VanNijnatten, D., 2021. Using indicators to assess transboundary water governance in the Great Lakes and Rio Grande-Bravo regions. Environ. Sustain. Indic. 10, 100102. https://doi.org/10.1016/j.indic.2021.100102

Khojasteh, D., Hottinger, S., Felder, S., Cesare, G. De, Heimhuber, V., Hanslow, D.J., Glamore, W., 2020. Estuarine tidal response to sea level rise: The significance of entrance restriction. Estuar. Coast. Shelf Sci. 244, 106941. https://doi.org/10.1016/j.ecss.2020.106941

Kinsela, M.A., Hanslow, D.J., Carvalho, R.C. et al. 2020. Mapping the Shoreface of Coastal Sediment Compartments to Improve Shoreline Change Forecasts in New South Wales, Australia. Estuaries and Coasts. https://doi.org/10.1007/s12237-020-00756-7

Liu, H., Yang, X., 2009. Shoreline Mapping and Coastal Change Studies Using remote sensing Imagery, in: Yang, X. (Ed.), Remote Sensing and Geospatial Technologies for Coastal Ecosystem

Assessment and Management. Berlin: Springer.

Lyard, F.H., Allain, D.J., Cancet, M., Carrère, L., Picot, N., 2020. FES2014 global ocean tides atlas: design and performances. Ocean Sci. Discuss. https://doi.org/https://doi.org/10.5194/os-2020-96

Mcfeeters, S.K., 1996. The use of the Normalized Difference Water Index ( NDWI ) in the delineation of open water features. Int. J. Remote Sens. 17, 1425–1432. https://doi.org/10.1080/01431169608948714

McPherson, B., Young, S., Modra, B., Couriel, E., You, B., Hanslow, D., Callaghan, D., Baldock, T., Nielsen, P., 2013. Penetration of tides and tidal anomalies in New South Wales estuaries. Coasts & Ports 2013, 537–542.

Mcsweeney, S.L., Kennedy, D.M., Rutherfurd, I.D., 2018. The daily-scale entrance dynamics of intermittently open/closed estuaries. Earth Surf. Process. Landforms 43, 791–807. https://doi.org/10.1002/esp.4280

Mcsweeney, S.L., Kennedy, D.M., Rutherfurd, I.D., Stout, J.C., 2017. Intermittently Closed/Open Lakes and Lagoons: Their global distribution and boundary conditions. Geomorphology. https://doi.org/10.1016/j.geomorph.2017.04.022

Mcsweeney, S.L., Stout, J.C., 2020. Variability in infragravity wave processes during estuary artificial entrance openings. Earth Surf. Process. Landforms 45, 3414–3428. https://doi.org/10.1002/esp.4974

Misra, A., Ramakrishnan, B., 2020. Assessment of coastal geomorphological changes using multi-temporal Satellite-Derived Bathymetry. Cont. Shelf Res. 207, 104213. https://doi.org/10.1016/j.csr.2020.104213

Monegaglia, F., Zolezzi, G., Güneralp, I., Henshaw, A.J., Tubino, M., 2018. Automated extraction of meandering river morphodynamics from multitemporal remotely sensed data. Environ. Model. Softw. 105, 171–186. https://doi.org/10.1016/j.envsoft.2018.03.028

Moore, L.J., Murray, A.B., 2018. Barrier dynamics and response to changing climate. Springer International Publishing AG. https://doi.org/10.1007/978-3-319-68086-6

Morris, B.D., Turner, I.L., 2010. Morphodynamics of intermittently open-closed coastal lagoon entrances: New insights and a conceptual model. Mar. Geol. 271, 55–66. https://doi.org/10.1016/j.margeo.2010.01.009

Mueller, N., Lewis, A., Roberts, D., Ring, S., Melrose, R., Sixsmith, J., Lymburner, L., McIntyre, A., Tan, P., Curnow, S., Ip, A., 2016. Water observations from space: Mapping surface water from 25 years of Landsat imagery across Australia. Remote Sens. Environ. 174, 341–352. https://doi.org/10.1016/j.rse.2015.11.003

Murray, N.J., Phinn, S.R., DeWitt, M., Ferrari, R., Johnston, R., Lyons, M.B., Clinton, N., Thau, D., Fuller, R.A., 2019. The global distribution and trajectory of tidal flats. Nature 565, 222–225. https://doi.org/10.1038/s41586-018-0805-8

Newton, A., Brito, A.C., Icely, J.D., Derolez, V., Clara, I., Angus, S., Schernewski, G., Inácio, M., Lillebø, A.I., Sousa, A.I., Béjaoui, B., Solidoro, C., Tosic, M., Cañedo-Argüelles, M., Yamamuro, M., Reizopoulou, S., Tseng, H.C., Canu, D., Roselli, L., Maanan, M., Cristina, S., Ruiz-Fernández, A.C., Lima, R.F. d., Kjerfve, B., Rubio-Cisneros, N., Pérez-Ruzafa, A., Marcos, C., Pastres, R., Pranovi, F., Snoussi, M., Turpie, J., Tuchkovenko, Y., Dyack, B., Brookes, J., Povilanskas, R., Khokhlov, V., 2018. Assessing, quantifying and valuing the ecosystem services of coastal lagoons. J. Nat. Conserv. 44, 50–65. https://doi.org/10.1016/j.jnc.2018.02.009

Niroumand-jadidi, M., Bovolo, F., Bruzzone, L., 2020. SMART-SDB : Sample-specific multiple band ratio technique for satellite- derived bathymetry. Remote Sens. Environ. 251, 112091. https://doi.org/10.1016/j.rse.2020.112091

Ohlendorf, S., Müller, A., Heege, T., Cerdeira-Estrada, S., Kobryn, H.T., 2011. Bathymetry mapping and sea floor classification using multispectral satellite data and standardized physics-based data processing., in: Remote Sensing of the Ocean, Sea Ice, Coastal Waters, and Large Water Regions 2011, 21 - 22 September, Prague. https://doi.org/10.1117/12.898652

Otvos, E.G., 2020. Coastal barriers - fresh look at origins, nomenclature and classification issues. Geomorphology 355, 107000. https://doi.org/10.1016/j.geomorph.2019.107000

Pardo-pascual, J.E., Almonacid-caballer, J., Ruiz, L.A., Palomar-vázquez, J., 2012. Automatic extraction of shorelines from Landsat TM and ETM+ multi-temporal images with subpixel precision. Remote Sens. Environ. 123, 1–11. https://doi.org/10.1016/j.rse.2012.02.024

Poliyapram, V., Raghavan, V., Metz, M., Delucchi, L., Masumoto, S., 2017. Implementation of Algorithm for Satellite-Derived Bathymetry using Open Source GIS and Evaluation for Tsunami Simulation. ISPRS Int. J. Geo-Information 6, 89. https://doi.org/10.3390/ijgi6030089

Poursanidis, D., Traganos, D., Reinartz, P., Chrysoulakis, N., 2019. On the use of Sentinel-2 for coastal habitat mapping and satellite-derived bathymetry estimation using downscaled coastal aerosol band. Int. J. Appl. Earth Obs. Geoinf. 80, 58–70. https://doi.org/10.1016/j.jag.2019.03.012

Ranasinghe, R., Pattiaratchi, C., 2003. The Seasonal Closure of Tidal Inlets: Causes and Effects. Coast. Eng. J. 45, 601–627. https://doi.org/10.1142/s0578563403000919

Roper, T., Creese, B., Scanes, P., Stephens, K., Williams, R., Dela-Cruz, J., Coade, G., Coates, B., Fraser, M., 2011. Assessing the condition of estuaries and coastal lake ecosystems in NSW, Monitoring, evaluation and reporting program, Technical report series. Sydney.

Rott, H., Cihlar, J., Schaepman, M.E., García-santos, G., Fernandes, R., Berger, M., 2012. Sentinels for science: Potential of Sentinel-1, -2, and -3 missions for scientific observations of ocean, cryosphere, and land. Remote Sens. Environ. 120, 91–101. https://doi.org/10.1016/j.rse.2011.09.026

Rowland, J.C., Shelef, E., Pope, P.A., Muss, J., Gangodagamage, C., Brumby, S.P., Wilson, C.J., 2016. A morphology independent methodology for quantifying planview river change and characteristics from remotely sensed imagery. Remote Sens. Environ. 184, 212–228. https://doi.org/10.1016/j.rse.2016.07.005

Roy, P.S., Williams, R.J., Jones, A.R., Yassini, I., Gibbs, P.J., Coates, B., West, R.J., Scanes, P.R., Hudson, J.P., Nichol, S., 2001. Structure and function of south-east Australian estuaries. Estuar. Coast. Shelf Sci. 53, 351–384. https://doi.org/10.1006/ecss.2001.0796

Ryu, J., Kim, C., Lee, Y., Won, J., Chun, S., Lee, S., 2008. Detecting the intertidal morphologic change using satellite data. Estuar. Coast. Shelf Sci. 78, 623–632. https://doi.org/10.1016/j.ecss.2008.01.020

Sagar, S., Roberts, D., Bala, B., Lymburner, L., 2017. Extracting the intertidal extent and topography of the Australian coastline from a 28 year time series of Landsat observations. Remote Sens. Environ. 195, 153–169. https://doi.org/10.1016/j.rse.2017.04.009

Sánchez-García, E., Palomar-Vázquez, J.M., Pardo-Pascual, J.E., Almonacid-Caballer, J., Cabezas-Rabadán, C., Gómez-Pujol, L., 2020. An efficient protocol for accurate and massive shoreline definition from mid-resolution satellite imagery. Coast. Eng. 160. https://doi.org/10.1016/j.coastaleng.2020.103732

Scanes, Peter R., Ferguson, A., Potts, J., 2020. Catastrophic events and estuarine connectivity influence presence of aquatic macrophytes and trophic status of intermittently-open coastal lagoons in eastern Australia. Estuar. Coast. Shelf Sci. 238, 106732. https://doi.org/10.1016/j.ecss.2020.106732

Schwenk, J., Khandelwal, A., Fratkin, M., Kumar, V., Foufoula-Georgiou, E., 2017. High spatiotemporal resolution of river planform dynamics from Landsat: The RivMAP toolbox and results from the Ucayali River. Earth Sp. Sci. 4, 46–75. https://doi.org/10.1002/2016EA000196

Siermann, J., Limited, G.T.L., Harvey, C., International, Q.S.U., Morgan, G., Solutions, S.G., Heege, T., 2014. Satellite Derived Bathymetry and Digital Elevation Models (DEM), in: International Petroleum Technology Conference Held in Doha, Qatar, 20–22 January 2014

Slinger, J.H., 2017. Hydro-morphological modelling of small, wave-dominated estuaries. Estuar. Coast. Shelf Sci. 198, 583–596. https://doi.org/10.1016/j.ecss.2016.10.038

Son, S., Paul, J., Lan, T., 2020. An optimal waterline approach for studying tidal flat morphological changes using remote sensing data : A case of the northern coast of Vietnam. Estuar. Coast. Shelf Sci. 236, 106613. https://doi.org/10.1016/j.ecss.2020.106613

Stephens, K., Murtagh, J., 2012. The Risky Business of ICOLL Entrance Management, in: 2012 Floodplain Management Association National Conference.

Turner, I.L., Harley, M.D., Drummond, C.D., 2016. UAVs for coastal surveying. Coast. Eng. 114, 19–24. https://doi.org/10.1016/j.coastaleng.2016.03.011

Van Der Walt, S., Schönberger, J.L., Nunez-Iglesias, J., Boulogne, F., Warner, J.D., Yager, N., Gouillart,

E., Yu, T., 2014. Scikit-image: Image processing in python. PeerJ 2014, 1–18. https://doi.org/10.7717/peerj.453

van Ormondt, M., Nelson, T.R., Hapke, C.J., Roelvink, D., 2020. Morphodynamic modelling of the wilderness breach, Fire Island, New York. Part I: Model set-up and validation. Coast. Eng. 157, 103621. https://doi.org/10.1016/j.coastaleng.2019.103621

Velasquez Montoya, L., Sciaudone, E.J., Mitasova, H., Overton, M.F., 2018. Observation and modeling of the evolution of an ephemeral storm-induced inlet: Pea Island Breach, North Carolina, USA. Cont. Shelf Res. 156, 55–69. https://doi.org/10.1016/j.csr.2018.02.002

Vos, K., Harley, M.D., Splinter, K.D., Simmons, J.A., Turner, I.L., 2019a. Sub-annual to multi-decadal shoreline variability from publicly available satellite imagery. Coast. Eng. 150, 160–174. https://doi.org/10.1016/j.coastaleng.2019.04.004

Vos, K., Harley, M.D., Splinter, K.D., Walker, A., Turner, I.L., 2020. Beach Slopes From Satellite-Derived Shorelines. Geophys. Res. Lett. 47. https://doi.org/10.1029/2020GL088365

Vos, K., Splinter, K.D., Harley, M.D., Simmons, J.A., Turner, I.L., 2019b. CoastSat: A Google Earth Engine-enabled Python toolkit to extract shorelines from publicly available satellite imagery. Environ. Model. Softw. 122, 104528. https://doi.org/10.1016/j.envsoft.2019.104528

Wainwright, D.J., Callaghan, D.P., Baldock, T.E., 2013. Statistical modelling of the barrier height fronting a coastal lagoon and the impact of sea-level rise. Coast. Eng. 75, 10–20. https://doi.org/10.1016/j.coastaleng.2013.01.003

Xu, H., 2007. Modification of normalised difference water index (NDWI) to enhance open water features in remotely sensed imagery 1161. https://doi.org/10.1080/01431160600589179

Young, S., Couriel, E., Jayewardene, I., McPherson, B., Clarke, G., 2014. Case study: Assessment of the entrance stability of the Lake Illawarra Estuary. Aust. J. Civ. Eng. https://doi.org/10.7158/C13-030.2014.12.1

Zhao, B., Guo, H., Yan, Y., Wang, Q., Li, B., 2008. A simple waterline approach for tidelands using multi-temporal satellite images: A case study in the Yangtze Delta. Estuar. Coast. Shelf Sci. 77,

134–142. https://doi.org/10.1016/j.ecss.2007.09.022

# InletTracker: An open-source Python toolkit for historic and near real-time monitoring of coastal inlets from Landsat and Sentinel-2

Valentin Heimhuber, Kilian Vos, Wanru Fu, William Glamore

## Supplementary material

### S1. Accuracy metrics used to assess the performance for predicting binary inlet states

After classifying the Δ-to-median series into binary open vs. closed inlet states, we first computed true positives (TP), false positives (FP), true negatives (TN) and false negatives (FN). We then calculated Accuracy as the fraction of all correct classifications over all samples in line with Equation 1 (Kotu and Deshpande, 2015). Open inlet states are considered 'positives' in these calculations.

$$Accuracy = (TP+TN)/(TP+FP+FN+TN) \quad \text{(Eq. 1)}$$

The F1 score is essentially a weighted average of precision and recall, where the precision is the proportion of correct positive cases to the tested positive cases. It reflects how precise the prediction is (Kotu and Deshpande, 2015).

$$Precision = TP/(TP+FP) \quad \text{(Eq. 2)}$$

In comparison, recall is the proportion of correct positive cases to real positive cases. It represents how well the system captures the targeted cases (Kotu and Deshpande, 2015).

$$Recall = TP/(TP+FN) \quad \text{(Eq. 3)}$$

The F1 score combines precision and recall together in the form of a harmonic mean that ranges between 0 and 1 (Kotu and Deshpande, 2015).

$$F1 = 2 \times (Precision \times Recall)/(Precision + Recall) \quad \text{(Eq. 4)}$$

## S2. Accuracy assessment results for high resolution monitoring of inlet dynamics via Sentinel-2 only (2016-2020)

**Table S1:** Validation statistics obtained via comparison of algorithm results against visually inferred inlet states for the S2 record only. Statistics are provided separately for the across-berm (A-B) and along-berm (C-D) transects. The number of images available for each site and number of open vs. closed visually inferred inlet states is also provided. The optimal classification threshold was used to classify images into open vs. closed states based on the Δ-to-median parameter, where Δ-to-median > threshold = open.

| Inlet site | Transect direction | F1-score | Accu-racy | True neg. | False pos. | False neg. | True pos. | Optimal classific. Threshold | Total nr. Of images | Nr. Of closed images | Nr. Of open images |
|---|---|---|---|---|---|---|---|---|---|---|---|
| Inmanriver | A-B | 0.71 | 0.79 | 65 | 11 | 14 | 31 | 0.01 | 121 | 76 | 45 |
| | C-D | 0.70 | 0.80 | 69 | 7 | 17 | 28 | 0.08 | - | - | - |
| Curl Curl | A-B | 0.65 | 0.90 | 149 | 9 | 9 | 17 | 0.01 | 184 | 158 | 26 |
| | C-D | 0.63 | 0.90 | 149 | 9 | 10 | 16 | 0.04 | - | - | - |
| Dee Why | A-B | 0.69 | 0.90 | 159 | 0 | 21 | 23 | 0.02 | 203 | 159 | 44 |
| | C-D | 0.66 | 0.87 | 150 | 9 | 18 | 26 | 0.03 | - | - | - |
| Coila | A-B | 1.00 | 1.00 | 119 | 0 | 0 | 6 | 0.01 | 125 | 119 | 6 |
| | C-D | 1.00 | 1.00 | 119 | 0 | 0 | 6 | 0.03 | - | - | - |
| Wamberal | A-B | 0.89 | 0.98 | 199 | 2 | 3 | 20 | 0.03 | 224 | 201 | 23 |
| | C-D | 0.91 | 0.98 | 199 | 2 | 2 | 21 | 0.04 | - | - | - |
| Narrabean | A-B | 0.98 | 0.98 | 59 | 3 | 0 | 65 | 0.09 | 127 | 62 | 65 |
| | C-D | 0.97 | 0.97 | 58 | 4 | 0 | 65 | 0.06 | - | - | - |
| Nadgee | A-B | 0.75 | 0.99 | 170 | 0 | 2 | 3 | 0.03 | 175 | 170 | 5 |
| | C-D | 0.33 | 0.95 | 165 | 5 | 3 | 2 | 0.15 | - | - | - |
| Hamersley Inlet | A-B | 1.00 | 1.00 | 96 | 0 | 0 | 1 | 0.02 | 97 | 96 | 1 |
| | C-D | 1.00 | 1.00 | 96 | 0 | 0 | 1 | 0.05 | - | - | - |
| Conjola | A-B | 0.94 | 0.95 | 48 | 1 | 4 | 42 | 0.01 | 95 | 49 | 46 |
| | C-D | 0.94 | 0.95 | 48 | 1 | 4 | 42 | 0.04 | - | - | - |
| Durras | A-B | 0.98 | 0.98 | 57 | 1 | 2 | 72 | 0.02 | 132 | 58 | 74 |
| | C-D | 0.99 | 0.98 | 58 | 0 | 2 | 72 | 0.09 | - | - | - |
| Stokes Inlet | A-B | 0.00 | 0.94 | 129 | 7 | 1 | 0 | 0.01 | 137 | 136 | 1 |
| | C-D | 0.00 | 0.58 | 80 | 56 | 1 | 0 | 0.01 | - | - | - |
| Irwin Inlet | A-B | 0.91 | 0.93 | 38 | 1 | 4 | 26 | 0.02 | 69 | 39 | 30 |
| | C-D | 0.92 | 0.93 | 36 | 3 | 2 | 28 | 0.02 | - | - | - |
| Average | A-B | 0.75 | 0.91 | - | - | - | - | 0.05 | 141 | 110 | 31 |
| Average | C-D | 0.79 | 0.94 | - | - | - | - | 0.02 | - | - | - |

## S3. Recommendations for optimal band and index selection

To account for the unique spectral characteristics of different coastal inlets, InletTracker currently provides NIR, SWIR1, NDWI and mNDWI as options for path finding and inferring of open vs. closed inlet states. These options are in line with the majority of state-of-the-art coastal shoreline or waterline mapping methods that either use a single band NIR or SWIR1/2 approach (Cabezas-Rabadán et al., 2020; Pardo-pascual et al., 2018; Ryu et al., 2002), or an approach based on a spectral index involving the green, NIR and/or SWIR bands (Bishop-taylor et al., 2019; Son et al., 2020; Vos et al., 2019). The performance of each of the four band/index options could not be explicitly tested as part of this work due to a lack of suitable in-situ validation data such as GPS transects. To provide recommendations in the absence of such data, a brief review of the relevant physical characteristics of the four options is provided here followed by a targeted analysis of six unique along-berm transects.

The reduced reflectance in the visible, NIR and SWIR wavelengths over water is the result of absorption and scattering of the electromagnetic radiation as it traverses the water column (Green et al., 2000). For pure water, the absorption of radiation increases exponentially from visible to NIR wavelengths and beyond (Green et al., 2000; Pope and Fry, 1997). For wavelengths above 1μm, such as those measured by the SWIR1 band, absorption is very high, even for turbid water (Liu et al., 2019). As a consequence, scattered puddles or wet mud that may be present in tidal flats can cause sufficient absorption in the SWIR range for exposed mudflats to be misclassified as standing water (Ryu et al., 2008). In the NIR band, on the other hand, there is a risk of shallow water areas being falsely classified as 'dry', due to lower absorption levels in water (compared to the SWIR range) and increased reflectance due to scattering in the presence of high suspended sediment content (Liu et al., 2019; Lodhi et al., 1997) and/or phytoplankton (Gitelson, 1992). Lastly, the NIR band is significantly affected by white water in the surf zone (Pardo-pascual et al., 2018; Ryu et al., 2002), which typically leads to elevated NIR reflectance (see across-berm paths avoiding white water in Figure 5) and the NDWI shifting towards the 'dry' range. Indices such as NDWI and mNDWI take advantage of the fact that attenuation in the green range is much lower than in the NIR or SWIR ranges consistently for a wide

range of different surface water features (Fisher et al., 2016; Mcfeeters, 1996; Xu, 2007). Both indices use the green band as part of a normalized difference ratio, so that their different behaviour largely corresponds to the aforementioned characteristics of the NIR and SWIR bands.

Many of the unique band and index features discussed above can be readily observed by analyzing NIR, SWIR1, NDWI and mNDWI transects over a common along-berm or across-berm path shown in Figure 9 for six example S2 images (three images during closed and three images during open inlet states). The higher sensitivity of the SWIR1 compared to the NIR band is illustrated well in the wider and deeper depressions over open inlets obtained for SWIR1. This is especially evident on the image of the 20-08-2020, where both the SWIR1 and the $mNDWI^{(-1)}$ indicate lower (in comparison to dry sand) values of around 0 for the tip of the southern berm adjacent to the channel (see solid blue lines). While this feature is, albeit less pronounced, also captured by the NIR band, it is lost in the NDWI. Unfortunately, it remains unclear whether the tip of the southern berm was covered with water or just wet sand in this example. Considering the tide level of 0.52m above mean sea level (AMSL) at the time of image capture (not shown), it is possible that shallow inundation was present around the transect in this section. The transects also illustrate that the normalized difference indices effectively eliminate the variability in reflectance that is present in both the SWIR1 and NIR bands over the dry berm areas along the path (see uneven and variable SWIR1 and NIR transects during closed inlets). In these dry berm areas, the NDWI and mNDWI indices exhibit stable values of around 0.2 and 0.3, respectively. Although these mean values can fluctuate from image to image due to lighting conditions and other factors (e.g., Figure 6e), this narrow spectral range is what enables our method to consistently infer the reflectance of dry berm areas via the median of the along-berm transect.

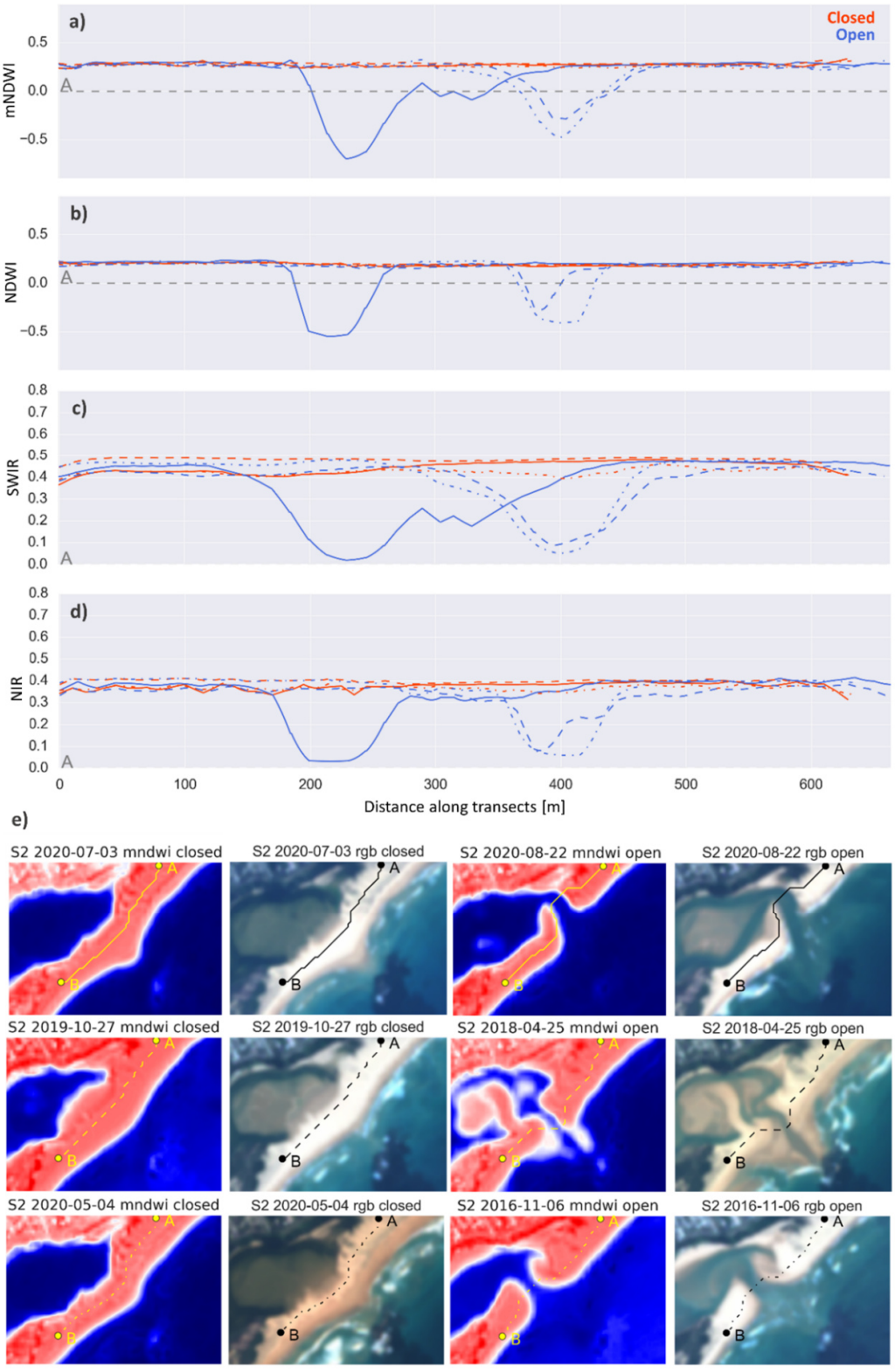


**Figure S1:** Comparison of NIR, SWIR1, NDWI and mNDWI for analysing inlet states based on three S2 images during open (blue lines) and three S2 images during closed inlet states (red lines).

Based on the physical characteristics discussed above and the experiments presented in this paper, we provide the following recommendations for inlet state detection via InletTracker.

- For pathfinding, it is advantageous to use either the NIR or SWIR1 band directly and use a mask to exclude heavily confounding classes such as vegetation or built-up areas.
- For inferring inlet states, on the other hand, it is recommended to use the normalized difference ratios as these provide a robust approximation of dry sand reflectance via the median of the along-berm transect.
- It is recommended to use the single band that corresponds to the index that is subsequently used for inferring inlet states (i.e., NIR/NDWI or SWIR1/mNDWI).
- The SWIR1/mNDWI approach provides a higher sensitivity for detecting very shallow or narrow inlet openings. Conversely, this high sensitivity to shallow waters and wet sand or mud can sometimes lead to falsely classifying a closed inlet as open.
- The NIR/NDWI approach is generally more conservative due to the lower sensitivity of the NIR band for very shallow waters. The low sensitivity to shallow waters can lead to classifying open inlet states as closed, especially when the image was acquired during low tide.
- For S2, the NIR band is of 10m resolution compared to 15m resolution of the SWIR1 band and as such, the S2 NIR/NDWI configuration is advantageous for IOCEs with small inlet channels.
- In the presence of highly turbid waters or large amounts of white water in or near the inlet channel, the SWIR1/mNDWI approach is likely to be more robust than the NIR/NDWI approach, due to the limited sensitivity of the SWIR1 band to these features.

In practice, we further recommend doing test runs for path finding using different seed and receiver point locations as well as band and index combinations. This will ensure that the optimal algorithm configuration is established before processing the full imagery archive.

115 **References**

116 Bishop-taylor, R., Sagar, S., Lymburner, L., Alam, I., Sixsmith, J., 2019. Sub-Pixel Waterline Extraction :
117 Characterising Accuracy and Sensitivity to Indices and Spectra. Remote Sens. 2019, 11, 2984.
118 https://doi.org/10.3390/rs11242984

119 Cabezas-Rabadán, C., Pardo-Pascual, J.E., Palomar-Vázquez, J.M., Fernández-Sarría, A., 2020. An efficient
120 protocol for accurate and massive shoreline definition from mid-resolution satellite imagery. Coast. Eng.
121 160. https://doi.org/10.1016/j.coastaleng.2020.103732

122 Fisher, A., Flood, N., Danaher, T., 2016. Comparing Landsat water index methods for automated water
123 classification in eastern Australia. Remote Sens. Environ. 175, 167–182.
124 https://doi.org/10.1016/j.rse.2015.12.055

125 Gitelson, A., 1992. The peak near 700 nm on radiance spectra of algae and water: relationships of its magnitude
126 and position with chlorophyll concentration. Int. J. Remote Sens. 13.
127 https://doi.org/10.1080/01431169208904125

128 Green, E.P., Mumby, P.J., Edwards, A.J., Clark, C.D., 2000. Remote Sensing Handbook for Tropical Coastal
129 Management, Remote Sensing Handbook for Tropical Coastal Management.
130 https://doi.org/10.1109/6.367967

131 Kotu, V., Deshpande, B., 2015. Model Evaluation, in: Predictive Analytics and Data Mining. https://doi.org/doi:
132 10.1016/b978-0-12-801460-8.00008-2.

133 Liu, H., Hu, S., Zhou, Q., Li, Q., Wu, G., 2019. Revisiting effectiveness of turbidity index for the switching scheme
134 of NIR- SWIR combined ocean color atmospheric correction algorithm. Int J Appl Earth Obs Geoinf. 76, 1–9.
135 https://doi.org/10.1016/j.jag.2018.10.010

136 Lodhi, M.A., Rundquist, D.C., Han, L., Kuzila, M.S., 1997. The potential for remote sensing of loewss soils
137 suspended in surface waters. J. Am. WATER Resour. Assoc. 33.

138 Mcfeeters, S.K., 1996. The use of the Normalized Difference Water Index (NDWI) in the delineation of open water
139 features. Int. J. Remote Sens. 17, 1425–1432. https://doi.org/10.1080/01431169608948714

140 Pardo-pascual, J.E., Elena, S., Almonacid-caballer, J., 2018. Assessing the Accuracy of Automatically Extracted
141 Shorelines on Microtidal Beaches from Landsat 7 , Landsat 8 and Sentinel-2 Imagery. Remote Sens. 10.

https://doi.org/10.3390/rs10020326

Pope, R.M., Fry, E.S., 1997. Absorption spectrum (380–700 nm) of pure water. II. Integrating cavity measurements. Appl. Opt. 36.

Ryu, J., Kim, C., Lee, Y., Won, J., Chun, S., Lee, S., 2008. Detecting the intertidal morphologic change using satellite data. Estuar. Coast. Shelf Sci. 78, 623–632. https://doi.org/10.1016/j.ecss.2008.01.020

Ryu, J., Won, J., Min, K.D., 2002. Waterline extraction from Landsat TM data in a tidal flat A case study in Gomso Bay , Korea 83, 442–456. https://doi.org/10.1016/S0034-4257(02)00059-7

Son, S., Paul, J., Lan, T., 2020. An optimal waterline approach for studying tidal flat morphological changes using remote sensing data: A case of the northern coast of Vietnam. Estuar. Coast. Shelf Sci. 236, 106613. https://doi.org/10.1016/j.ecss.2020.106613

Vos, K., Harley, M.D., Splinter, K.D., Simmons, J.A., Turner, I.L., 2019. Sub-annual to multi-decadal shoreline variability from publicly available satellite imagery. Coast. Eng. 150, 160–174. https://doi.org/10.1016/j.coastaleng.2019.04.004

Xu, H., 2007. Modification of normalised difference water index (NDWI) to enhance open water features in remotely sensed imagery 1161. https://doi.org/10.1080/01431160600589179